ARCHIVES OF MECHANICS
Arch. Mech. **74** (6), 463–511, 2022, DOI: 10.24423/aom.4150

Free vibration analysis of porous functionally graded piezoelectric microplates resting on an elastic medium subjected to electric voltages

C.-P. WU, E.-L. LIN

Department of Civil Engineering, National Cheng Kung University, Tainan 10701, Taiwan,
e-mails: cpwu@mail.ncku.edu.tw (corresponding author), simon870914@gmail.com

Basing on the consistent couple stress theory (CCST), we develop a unified size-dependent shear deformation theory to analyze the free vibration characteristics of simply supported, porous functionally graded (FG) piezoelectric microplates which resting on the Winkler–Pasternak foundation are subjected to electric voltages. Various CCST-based shear deformation theories can be reproduced by incorporating their corresponding shape functions, which characterize the through-thickness distributions of the shear deformations, into the unified size-dependent theory. The reproduced CCST-based plate theories include the classical plate theory (CPT), the first-order shear deformation plate theory (SDPT), Reddy's refined SDPT, the sinusoidal SDPT, the exponential SDPT, and the hyperbolic SDPT. The unified size-dependent theory is subsequently used to determine the natural frequencies of simply supported, porous FG piezoelectric microplates and their corresponding vibration mode shapes. The effects of the material length scale parameter, the length-to-thickness ratio, the material-property gradient index, different values of the applied voltages, the porosity parameter, different porosity distribution patterns, the Winkler spring coefficient, and the shear modulus of the surrounding medium on the natural frequencies of the porous FG piezoelectric microplates are examined and appear to be significant.

Key words: consistent couple stress theory, functionally graded material, the Winkler–Pasternak Foundation, piezoelectric microplates, porous microplates, vibration.

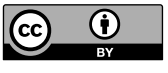

1. Introduction

In recent decades, piezoelectric materials have become important in industrial applications. The benefits that these materials bring are derived from the direct piezoelectric effect and the converse piezoelectric effect, which cause mechanical energy to be converted into electrical energy and electric energy to be converted into mechanical energy, respectively [1]. In other words, when a piezoelectric structure is subjected to mechanical loads, it undergoes a mechanical deformation as positive and negative charges of the same magni-

tude are generated on its opposite surfaces. The phenomenon of electrical polarization being caused by such a mechanical deformation is called the direct piezoelectric effect. On the other hand, the application of an electric voltage to the surface of a piezoelectric material increases the distance of the electric dipole causing this material to lengthen in the direction of the electric field. The phenomenon of a mechanical deformation being caused by the action of the electric voltage is called the converse piezoelectric effect. In view of such excellent bidirectional conversion capabilities, piezoelectric materials are widely used in various cutting-edge technologies, including sensors, actuators, control systems, micro-electro-mechanical systems (MEMSs), and nano-electro-mechanical systems (NEMSs). Accordingly, various analytical and numerical methods based on classical continuum mechanics (CCM) have been developed in investigations of the coupled electro-mechanical behavior of piezoelectric plates with the goals of prolonging their service life and providing a reference for their structural design. Comprehensive reviews of the literature have been conducted to assess the scope of the application of such analytical and numerical methods. The reviewed research has examined the coupled electro-mechanical behavior of laminated composite piezoelectric plates and functionally graded (FG) piezoelectric plates on the basis of the following two-dimensional (2D) and three-dimensional (3D) plate theories based on the CCM: the classical plate theory (CPT), the first-order shear deformation plate theory (FSDPT), Reddy's refined shear deformation plate theory (RSDPT), the third-order shear deformation plate theory (TSDPT), the sinusoidal shear deformation plate theory (SSDPT), the exponential shear deformation plate theory (ESDPT), the hyperbolic shear deformation plate theory (HSDPT), and the 3D theory of piezoelectricity [2–8].

With the fields of precision manufacturing, materials science, and materials technology developing rapidly, the dimensions of various industrial components and devices have reached the scales of the micron (or 10^{-6} m) and the nanometer (or 10^{-9} m). Because of their direct and converse piezoelectric effects, the piezoelectric material microplate (PMMP) has a great potential for a wide range of applications in cutting edge technologies. For example: PMMP has been adopted as a resonator in telecommunications and biotechnologies, it is used in some devices which are: film buck acoustic wave resonators, microplate resonators, microcantilevers, and microbridges [9, 10]; PMMP has been adopted as an oscillator featuring an in-liquid piezoelectric microplate resonator as the frequency-selective element for density and viscosity sensing [11]; and PMMP has been adopted as an actuator in micropumps [12, 13]. In addition, piezoelectric material has also been used to form some micro-sized instruments to promote cell adhesion and spreading, including micropipets, microneedles, and microspheres [14]. Some other applications of piezoelectric materials in macroscopic, microscopic, and nanoscale smart structures can refer to Qiu and Ji [15].

The use of the CCM-based analytical and numerical methods mentioned above for analyzing FG piezoelectric macroplates is no longer feasible due to the size effect, which is significant when the dimensions of the piezoelectric structure is shrunk to such small scales. Work carried out by TOUPIN [16], MINDLIN and TIERSTEN [17], and KOITER [18] forms the foundation of the couple stress theory (CST), the so-called Toupin–Mindlin–Koiter CST (TMK-CST), which was developed in order to account for the size effect in the analysis of various mechanical behaviors of elastic microscale bodies. The TMK-CST introduced a macro-rotation tensor to account for the true kinematics of rotational motion in the CCM. However, some theoretical inconsistencies were encountered when the TMK-CST was implemented, including the indeterminacy of the spherical part of the couple-stress tensor and the appearance of the body couple in the constitutive relation for the force-stress tensor [19], the further development of the TMK-CST and its application have been suspended for the time being.

In order to overcome the shortcomings of the TMK-CST, YANG *et al.* [20] developed a modified couple stress theory (MCST) for the analysis of elastic microscale bodies. In their formulation, the couple-stress tensor was considered to be a symmetric tensor conjugated with the symmetric part of the curvature tensor which contributes significantly to the total strain energy of the system, and an additional equilibrium relation was derived to govern the mechanical behavior of the elastic microscale bodies which is attributable to the moment of the couple. The MCST was then used to demonstrate that it is a feasible model for examining the torsion behavior of a cylindrical bar and the pure bending behavior of a flat plate of an infinite width. As a result, various size-dependent plate theories based on the MCST have been developed for analyzing the mechanical behaviors of laminated composite elastic microplates and FG elastic microplates, such as the MCST-based CPT [21–24], the MCST-based FSDPT [23, 25], the MCST-based RSDPT [26, 27], and the MCST-based SSDPT [28].

The MCST has also been applied to the analysis of the coupled electro-mechanical behavior of FG piezoelectric microbeams and microplates. Incorporating the kinematic model of the Euler–Bernoulli beam theory into the MCST, BENI and BENI [29] analyzed the dynamic stability behavior of size-dependent viscoelastic/piezoelectric nanobeams, with the effect of von Kármán geometrical nonlinearity taking into consideration. In conjunction with the kinematic model of the Timoshenko beam theory and the CCST, BENI [30] studied the static bending behavior of piezoelectric nanobeams subjected to electro-mechanical loads. Combining the MCST with the displacement model of the CPT, JAFARI *et al.* [31] investigated the free vibration characteristics of sandwich piezoelectric microplates, and KAZEMI *et al.* [32] examined the free vibration characteristics of FG microplates subjected to electrostatic and piezoelectric excitations. Basing on the MCST-based CPT, AKGÖZ and CIVALEK [33] presented the ana-

lytical solutions for bending, buckling, and vibration of microplates on an elastic medium. In conjunction with the kinematic model of a refined plate theory (RPT) and the MCST, Pham and Nguyen [34] developed a four-variable RPT-based isogeometric analytical method for analyzing the dynamic stability behavior of porous FG microplates. Ghobadi *et al.* [35] presented a size-dependent thermo-electro-mechanical nonlinear bending analysis of nanoplates using the modified flexoelectric theory (MFT), with the kinematic model of the CPT. The MFT-based CPT was also applied to examine the size-dependent nonlinear thermo-electro-mechanical free vibration characteristics of FG flexoelectric nanoplates [36], to study the static bending behavior of porous flexoelectric cylindrical nanoshells [37], and to investigate the nonlinear vibration characteristics of FG porous nanostructures, with the porosity distribution effect taking into consideration [38].

Eringen's nonlocal elasticity theory (ENET) has been applied to various mechanical analyses of porous FG nanoplates. Basing on the Hamilton principle, Pham et al. [39] developed a four-node quadrilateral element with ten degrees of freedom for each node for examining the bending and hygro-thermo-mechanical vibration characteristics of porous sandwich FG doubly curved nanoshells resting on the Winkler–Pasternak foundation. Pham *et al.* [40] developed an improved triangular element based on the FSDT to investigate the static bending, free vibration, and buckling behavior of porous FG nanoplates resting on the Winkler–Pasternak foundation. Basing on the ENET combined with the kinematic model of FSDT, Pham *et al.* [41] developed 3-node triangular element to study the free vibration characteristics of porous FG annular nanoplates resting on the Winkler foundation. Based on the ENET, Pham *et al.* [42] presented a dynamic analysis for porous FG sandwich nanoplates using a higher-order isogeometric analytical method.

Lou *et al.* [43] analyzed the buckling and post-buckling behaviors of sandwich piezoelectric microplates subjected to thermo-electro-mechanical loads using a size-dependent FSDPT based on the MCST. This approach has also been used to examine both the shear buckling behavior of piezoelectric nanoplates by Malikan [44] and the thermo-electro-mechanical buckling characteristics of FG graphene platelets-reinforced composite (GPLRC) sandwich microplates by Abbaspour and Arvin [45]. Incorporating the first-order shear deformation model into the MCST, Safarpour *et al.* [46] investigated the thermal buckling and the free and forced vibration behaviors of FG-GPLRC nanoscale cylindrical shells which were subjected to hydraulic pressure and thermal loads resting on the Winkler–Pasternak foundation. Li and Pan [47] developed a size-dependent SSDPT based on the MCST to study the static bending and free vibration behaviors of FG piezoelectric microplates subjected to electric voltages and mechanical loads acting on the top and bottom surfaces of the microplates. Com-

bining the MCST with a four-variable shear deformation theory, ABAZID and SOBHY [48] studied the coupled thermo-electro-mechanical bending behavior of FG piezoelectric microplates resting on the Winkler–Pasternak foundation, and NGUYEN and LEE [49] conducted an analysis of the static bending and free vibration behaviors of FG-GPLRC piezoelectric microplates. In conjunction with the MCST and Timoshenko's beam model, ESHRAGHI and DAG [50] developed a domain-boundary element method for transient dynamic analysis of FG microbeams with considering small-scale effects. Incorporating the MCST with the Euler–Bernoulli beam model, RAZEGHI-HARIKANDEEI *et al.* [51] studied the delamination effect on the static bending, free vibration, and forced vibration behavior of a delaminated microbeam-based MEMS subjected to the nonlinear electrostatic force. Finally, KARIMIPOUR *et al.* [52] developed a generalized differential quadrature (GDQ) method for the 3D static bending and free vibration analyses of micro-sized torus panels, for which a general curvilinear coordinate system was used to derive the formulation, such that it can be applied to various mechanical analyses of irregular geometries, cap-shaped panels, saddle-shaped panels, and sectional-shaped panels.

In response to the problematic nature of the TMK-CST, HADJESFANDIARI and DARGUSH [53, 54] and HADJESFANDIARI [55] developed a new version of the CST, the consistent couple stress theory (CCST), which was applied to the analysis of elastic microscale bodies and piezoelectric microscale bodies, respectively. In these studies, the couple-stress tensor was a skew-symmetric tensor, conjugated with the skew-symmetric part of the curvature tensor, with the skew-symmetric couple-stress tensor and the skew-symmetric curvature tensor contributing significantly to the total strain energy of the system. It should be noted that in the formulation of the CCST applied to the analysis of piezoelectric bodies, the effects of flexoelectricity, piezoelectricity, and the material length scale parameter on the coupled electro-mechanical behavior of piezoelectric bodies were accounted for.

Based on the CCST and the MCST, some size-dependent plate/beam theories have also been developed for investigating the coupled electro-mechanical behavior of FG piezoelectric microplates/microshells, with the piezoelectric effect being considered. For instance, ABBASPOUR and ARVIN [56] developed a CCST-based CPT for analyzing the vibration and thermal buckling behaviors of three-layered piezoelectric microplates. Incorporating the CCST and the Donnell shell theory, RAZAVI *et al.* [57] and ZENG *et al.* [58] investigated the free vibration and static buckling behaviors of FG piezoelectric nanoscale cylindrical shells, respectively, for which the piezoelectric effect, the material length scale parameter effect, and the material-property gradient index effect on the frequency parameters and the critical load parameters of piezoelectric microplates and piezoelectric microshells were examined.

After a close survey of the relevant literature, we found no studies examining the issue of interest here, namely the analysis of the free vibration behavior of simply-supported, porous FG piezoelectric microplates which rest on the Winkler–Pasternak foundation and are subjected to electric voltages in the context of electro-mechanical coupling. Wu and Hu [59] did develop a unified size-dependent theory based on the CCST to analyze the static bending and free vibration behaviors of FG elastic microplates, rather than FG piezoelectric microplates. Therefore, in this work we aim to develop a CCST-based unified size-dependent theory to be applied to the study of porous FG piezoelectric microplates. Basing on Hamilton's principle, we derive the Euler–Lagrange equations of FG piezoelectric microplates and their corresponding possible boundary conditions. Accordingly, the derived Euler–Lagrange equations are used to obtain the natural frequencies of simply-supported, porous FG piezoelectric microplates and their corresponding vibration mode shapes on the basis of Navier's method. A number of key effects on the natural frequencies of the porous FG piezoelectric microplates are investigated, including the material length scale parameter, the length-to-thickness ratio, the material-property gradient index, different values of the applied voltages, the porosity parameter, different porosity distribution patterns, the Winkler spring coefficient, and the shear modulus of the medium surrounding the microplate.

2. Formulations

In this work, by integrating the CCST applied to the analysis of piezoelectric microscale bodies together with Hamilton's principle, we aim to develop a unified size-dependent theory to examine the free vibration characteristics of simply-supported, porous FG piezoelectric microplates resting on the Winkler–Pasternak foundation and are subjected to electric voltages acting on the top and bottom surfaces. The properties of the microplate material are assumed to obey a power–Law distribution of the volume fractions of the constituents in the direction of the thickness of the microplates, and the effective material properties are estimated using the rule of mixtures. The distribution of the porosity in the direction of the thickness of the microplates is categorized into two types, Types A and B. Regarding the former, the functions for three patterns of porosity distribution are considered for the purposes of comparison, and for the latter, the functions for four porosity distribution patterns are used in a parametric study presented in a later section of this paper. A schematic diagram of the kind of porous FG piezoelectric microplate of interest in this study is shown in Fig. 1, with the electric voltages V_0 and $-V_0$ applied to the top and bottom surfaces, respectively. The electric potentials and the stress tractions acting on the edges of the microplate are set to zero.

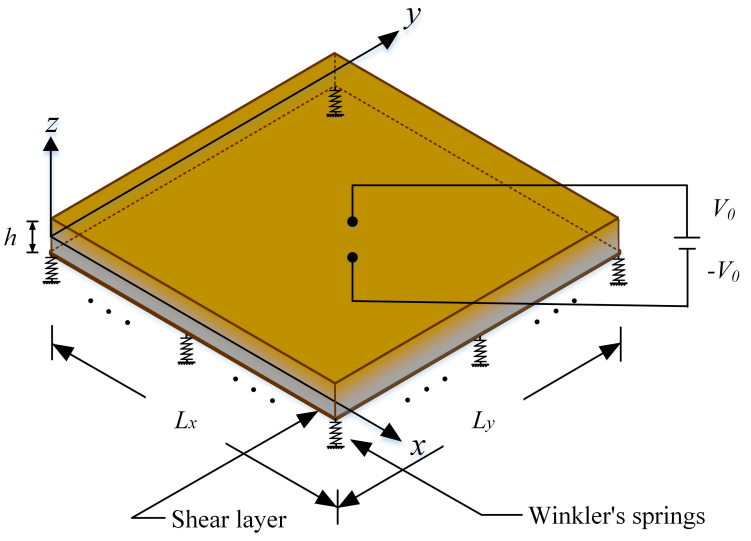

FIG. 1. A schematic diagram of a porous FG piezoelectric microplate which resting on the Winkler–Pasternak foundation is subjected to electric voltages.

As mentioned above, HADJESFANDIARI and DARGUSH [53, 54] first developed a CCST for analyzing elastic microscale bodies, which HADJESFANDIARI [55] subsequently applied to address the analysis of a piezoelectric microscale body. Hadjesfandiari and Dargush indicated that the force-stress tensor (σ_{ij}) induced at a material point in a deformed piezoelectric microscale body was asymmetric and the couple-stress tensor (μ_{ij}) was skew-symmetric. The force-stress tensor was thus decomposed into its symmetric ($\sigma_{(ij)}$) and skew-symmetric ($\sigma_{[ij]}$) parts, which were represented using parentheses and brackets surrounding the pair of indices, respectively.

According to Hadjesfandiari's derivation, the skew-symmetric part of the force-stress tensor can be expressed in terms of the couple-stress tensor as follows:

$$\sigma_{[ji]} = -\tfrac{1}{2}(\mu_{i,j} - \mu_{j,i}), \tag{2.1}$$

where $\mu_k = \mu_{ji} = -\mu_{ij}$, and the subscripts i, j, and k permute in a natural order.

The strain energy density function of a piezoelectric microscale solid is a function of the strain tensor (ε_{ij}), the skew-symmetric part of the curvature tensor (κ_{ij}), and the electric field tensor (E_k). The strain tensor is symmetric and conjugated with the symmetric part of the force-stress tensor ($\sigma_{(ij)}$), the skew-symmetric part of the curvature tensor is conjugated with the couple-stress tensor (μ_{ij}), and the electric field tensor is conjugated with the electric displace-

ment (flux) tensor (D_k). The strain energy density function in a piezoelectric microscale body occupying a volume Ω can thus be written as follows:

$$U_s = \int_{\Omega} \left[\tfrac{1}{2}\sigma_{(ij)}\varepsilon_{ij} - \mu_{ij}\kappa_{ij} - \tfrac{1}{2}D_k E_k\right] d\Omega. \tag{2.2}$$

2.1. Generalized kinematics

In this unified size-dependent theory for analyzing a porous FG piezoelectric microplate, the components of the generalized displacement are expressed as follows:

$$u_x(x,y,z,t) = u(x,y,t) - z\frac{\partial w(x,y,t)}{\partial x} + f(z)\gamma_x(x,y,t), \tag{2.3}$$

$$u_y(x,y,z,t) = v(x,y,t) - z\frac{\partial w(x,y,t)}{\partial y} + f(z)\gamma_y(x,y,t), \tag{2.4}$$

$$u_z(x,y,z,t) = w(x,y,t), \tag{2.5}$$

$$\Phi(x,y,z,t) = -g(z)\phi(x,y,t) + (2zV_0/h), \tag{2.6}$$

where u, v, and w represent the mid-plane displacements of the microplate in the x, y, and z directions, respectively; ϕ is defined as the mid-plane electric potential of the microplate; and γ_x and γ_y denote the mid-plane shear rotations of the microplate in the xz-plane and yz-plane, respectively. The values of V_0 and $-V_0$ are the constant electric voltages applied to the top and the bottom surfaces of the microplate, respectively. The form of $g(z)$ is given as $g(z) = \cos(\pi z/h)$. The assumed form of $\Phi(x,y,z,t)$ presented in Eq. (2.6) was first proposed by Wang [60], and in subsequent work by Wang *et al.* [61], it was validated along with the natural frequency parameters of a piezoelectric plate obtained using a theoretical model and the finite element method. The assumed form of Φ has since been commonly used by other researchers [35, 43, 47, 48]. The through-thickness distribution of the transverse shear deformations is characterized by $f(z)/dz$, for which $f(z)$ denotes a specific function of z. The generalized displacement fields of the CPT and various SDPTs can be obtained by defining $f(z)$ as follows:

$$\text{CPT}: \quad f(z) = 0, \tag{2.7}$$

$$\text{FSDPT}: \quad f(z) = z, \tag{2.8}$$

$$\text{RSDPT}: \quad f(z) = z - [(4z^3)/(3h^2)], \tag{2.9}$$

$$\text{SSDPT}: \quad f(z) = (h/\pi)\sin(\pi z/h), \tag{2.10}$$

$$\text{ESDPT}: \quad f(z) = ze^{-(2z^2/h^2)}, \tag{2.11}$$

$$\text{HSDPT}: \quad f(z) = z\cosh(1/2) - h\sinh(z/h). \tag{2.12}$$

The strain-displacement relations of the microplate are given as:

$$\varepsilon_{xx} = u_{,x} - zw_{,xx} + f\gamma_{x,x}\,, \tag{2.13}$$

$$\varepsilon_{yy} = v_{,y} - zw_{,yy} + f\gamma_{y,y}\,, \tag{2.14}$$

$$\varepsilon_{zz} = 0, \tag{2.15}$$

$$\gamma_{xz} = (Df)\gamma_x, \tag{2.16}$$

$$\gamma_{yz} = (Df)\gamma_y, \tag{2.17}$$

$$\gamma_{xy} = u_{,y} + v_{,x} - 2zw_{,xy} + f(\gamma_{x,y} + \gamma_{y,x}), \tag{2.18}$$

where the commas in Eqs. (2.13)–(2.18) represent the derivative of the suffix variable, and $Df = df(z)/dz$.

The relationship between the electric field and the electric potential of the microplate is expressed as:

$$E_x = g\phi_{,x}\,, \tag{2.19}$$

$$E_y = g\phi_{,y}\,, \tag{2.20}$$

$$E_z = (Dg)\phi - (2V_0/h), \tag{2.21}$$

where $Dg = dg(z)/dz$.

The rotation-displacement relationship of the microplate is expressed as:

$$\boldsymbol{\theta} = \theta_x\mathbf{i} + \theta_y\mathbf{j} + \theta_z\mathbf{k} = \tfrac{1}{2}\,\mathrm{curl}(\mathbf{u}), \tag{2.22}$$

where $\mathbf{i}$, $\mathbf{j}$, and $\mathbf{k}$ denote the unit base vectors in the x, y, and z directions, respectively, and:

$$\mathbf{u} = u_x\mathbf{i} + u_y\mathbf{j} + u_z\mathbf{k}, \tag{2.23}$$

$$\theta_x = \theta_{zy} = \tfrac{1}{2}[2w_{,y} - (Df)\gamma_y], \tag{2.24}$$

$$\theta_y = \theta_{xz} = \tfrac{1}{2}[-2w_{,x} + (Df)\gamma_x], \tag{2.25}$$

$$\theta_z = \theta_{yx} = \tfrac{1}{2}[(v_{,x} - u_{,y}) + f(\gamma_{y,x} - \gamma_{x,y})]. \tag{2.26}$$

The symmetric part of the curvature tensor of the microplate is expressed as:

$$\chi_{xx} = \theta_{x,x} = \tfrac{1}{2}[2w_{,xy} - (Df)\gamma_{y,x}], \tag{2.27}$$

$$\chi_{yy} = \theta_{y,y} = \tfrac{1}{2}[-2w_{,xy} + (Df)\gamma_{x,y}], \tag{2.28}$$

$$\chi_{zz} = \theta_{z,z} = \tfrac{1}{2}[(Df)(\gamma_{y,x} - \gamma_{x,y})], \tag{2.29}$$

$$\chi_{xz} = \tfrac{1}{2}(\theta_{x,z} + \theta_{z,x}) = \tfrac{1}{4}[(v_{,xx} - u_{,xy}) + f(\gamma_{y,xx} - \gamma_{x,xy}) - (D^2f)\gamma_y], \tag{2.30}$$

$$\chi_{yz} = \tfrac{1}{2}(\theta_{y,z} + \theta_{z,y}) = \tfrac{1}{4}[(v_{,xy} - u_{,yy}) + f(\gamma_{y,xy} - \gamma_{x,yy}) + (D^2f)\gamma_x], \tag{2.31}$$

$$\chi_{xy} = \tfrac{1}{2}(\theta_{x,y} + \theta_{y,x}) = \tfrac{1}{4}[2(w_{,yy} - w_{,xx}) + (Df)(\gamma_{x,x} - \gamma_{y,y})], \tag{2.32}$$

where $D^2f = d^2f/dz^2$.

The skew-symmetric part of the curvature tensor $\boldsymbol{\kappa}$ of the microplate is expressed as:

$$\boldsymbol{\kappa} = \kappa_x \mathbf{i} + \kappa_y \mathbf{j} + \kappa_z \mathbf{k} = \tfrac{1}{2}\,\mathrm{curl}(\boldsymbol{\theta}), \tag{2.33}$$

where

$$\kappa_x = \kappa_{zy} = \tfrac{1}{4}[(v_{,xy} - u_{,yy}) + f(\gamma_{y,xy} - \gamma_{x,yy}) - (D^2 f)\gamma_x], \tag{2.34}$$

$$\kappa_y = \kappa_{xz} = \tfrac{1}{4}[(u_{,xy} - v_{,xx}) + f(\gamma_{x,xy} - \gamma_{y,xx}) - (D^2 f)\gamma_y], \tag{2.35}$$

$$\kappa_z = \kappa_{yx} = \tfrac{1}{4}[-2(w_{,xx} + w_{,yy}) + (Df)(\gamma_{x,x} + \gamma_{y,y})]. \tag{2.36}$$

2.2. Generalized constitutive equations

As aforementioned, in this work we consider two types of porosity distributions in the direction of the thickness of the microplate, Types A and B. In the case of Type A, the functions of three patterns of the porosity distribution are considered for the purposes of comparison, and for Type B, the functions of four distribution patterns are considered for a parametric study. These functions are held to represent the volume fraction of the porosity, $\psi(z)$, and they are presented in the following sections for both types of distributions in addition to their corresponding effective material properties, $P(z)$.

For Types A-1, A-2, and A-3, the functions of the porosity distribution through the thickness of the microplate are expressed as:

$$\text{Type A-1:} \quad \psi(z) = \psi_0, \tag{2.37a}$$

$$\text{Type A-2:} \quad \psi(z) = \psi_0[1 - (2|z|/h)], \tag{2.37b}$$

$$\text{Type A-3:} \quad \psi(z) = \psi_0\left[\tfrac{1}{2} - (|z|/h)\right]^{\kappa_\psi}, \tag{2.37c}$$

where ψ_0 denotes the porosity parameter; κ_ψ denotes the porosity gradient index. The functions of the volume fractions of the porosity for Type A-1 and A-2 are taken from Barati *et al.* [62] and that for Type A-3 from Karamanli and Aydogdu [63].

The effective material properties of Types A-1, A-2, and A-3, following the formulation devised by Shafiei *et al.* [64], are expressed as:

$$\begin{aligned} P(z) &= P_t[V_t - (\psi(z)/2)] + P_b[V_b - (\psi(z)/2)] \\ &= (P_t - P_b)V_t + P_b - [(P_t + P_b)\psi(z)/2], \end{aligned} \tag{2.38}$$

where the volume fraction of the porosity is assumed to be equally distributed throughout the constituent materials of the microplate; the subscripts t and b represent the top and bottom surfaces of the microplate, respectively; P_t and P_b denote the material properties of the top and bottom surfaces of the microplate,

respectively; V_t and V_b denote the volume fractions of the constituent materials on the top and bottom surfaces of the microplate, respectively; $V_t = \left[\frac{1}{2} + (z/h)\right]^{\kappa_p}$; $V_t + V_b = 1$; and κ_p represents the material-property gradient index. In the work of KARAMANLI and AYDOGDU [63], the porosity gradient index (κ_ψ) and the material-property gradient index (κ_p) were assumed to be identical.

For Types B-1, B-2, B-3, and B-4, the functions of the volume fractions of the porosity through the thickness of the microplate are expressed as:

$$\text{Type B-1:} \quad \psi(z) = 2\psi_0/\pi, \tag{2.39a}$$

$$\text{Type B-2:} \quad \psi(z) = \psi_0 \cos(\pi z/h), \tag{2.39b}$$

$$\text{Type B-3:} \quad \psi(z) = \psi_0 \cos\{(\pi/2)[(z/h) + (1/2)]\}, \tag{2.39c}$$

$$\text{Type B-4:} \quad \psi(z) = \psi_0 \cos\{(\pi/2)[(z/h) - (1/2)]\}, \tag{2.39d}$$

with the functions for Types B-2, B-3, and B-4 taken from KIM *et al.* [25]. Because the pore volumes of these four Types remain constant, they can be used for a parametric study in a later part of this paper, where the pore volumes are expressed as:

$$\int_{-h/2}^{h/2} \psi(z)\, dz = \frac{2h\psi_0}{\pi}.$$

The effective material properties of Types B-1, B-2, B-3, and B-4 are expressed following KIM *et al.* [25] as:

$$P(z) = [(P_t - P_b)V_t + P_b][1 - \psi(z)], \tag{2.40}$$

where $V_t = \left[\frac{1}{2} + (z/h)\right]^{\kappa_p}$.

Based on the plane stress assumptions, the generalized constitutive equations of the microplate composed of an FG piezoelectric orthotropic material can be expressed following HADJESFANDIARI [55] as:

$$\begin{Bmatrix} \sigma_{(xx)} \\ \sigma_{(yy)} \\ \sigma_{(xy)} \\ \sigma_{(yz)} \\ \sigma_{(xz)} \end{Bmatrix} = \begin{bmatrix} \bar{c}_{11} & \bar{c}_{12} & 0 & 0 & 0 \\ \bar{c}_{12} & \bar{c}_{22} & 0 & 0 & 0 \\ 0 & 0 & c_{66} & 0 & 0 \\ 0 & 0 & 0 & c_{44} & 0 \\ 0 & 0 & 0 & 0 & c_{55} \end{bmatrix} \begin{Bmatrix} \varepsilon_{xx} \\ \varepsilon_{yy} \\ \gamma_{xy} \\ \gamma_{yz} \\ \gamma_{xz} \end{Bmatrix} - \begin{bmatrix} 0 & 0 & \bar{e}_{31} \\ 0 & 0 & \bar{e}_{32} \\ 0 & 0 & 0 \\ 0 & e_{24} & 0 \\ e_{15} & 0 & 0 \end{bmatrix} \begin{Bmatrix} E_x \\ E_y \\ E_z \end{Bmatrix} + \begin{bmatrix} 0 & 0 & \bar{d}_{31} \\ 0 & 0 & \bar{d}_{32} \\ 0 & 0 & 0 \\ 0 & d_{24} & 0 \\ d_{15} & 0 & 0 \end{bmatrix} \begin{Bmatrix} \kappa_x \\ \kappa_y \\ \kappa_z \end{Bmatrix}, \tag{2.41}$$

$$\begin{Bmatrix} D_x \\ D_y \\ D_z \end{Bmatrix} = \begin{bmatrix} 0 & 0 & 0 & 0 & e_{15} \\ 0 & 0 & 0 & e_{24} & 0 \\ \bar{e}_{31} & \bar{e}_{32} & 0 & 0 & 0 \end{bmatrix} \begin{Bmatrix} \varepsilon_{xx} \\ \varepsilon_{yy} \\ \gamma_{xy} \\ \gamma_{yz} \\ \gamma_{xz} \end{Bmatrix} + \begin{bmatrix} \eta_{11} & 0 & 0 \\ 0 & \eta_{22} & 0 \\ 0 & 0 & \bar{\eta}_{33} \end{bmatrix} \begin{Bmatrix} E_x \\ E_y \\ E_z \end{Bmatrix} + \begin{bmatrix} a_{11} & 0 & 0 \\ 0 & a_{22} & 0 \\ 0 & 0 & \bar{a}_{33} \end{bmatrix} \begin{Bmatrix} \kappa_x \\ \kappa_y \\ \kappa_z \end{Bmatrix}, \tag{2.42}$$

$$\begin{Bmatrix} \mu_x \\ \mu_y \\ \mu_z \end{Bmatrix} = -\frac{1}{2} \begin{bmatrix} 0 & 0 & 0 & 0 & d_{15} \\ 0 & 0 & 0 & d_{24} & 0 \\ \bar{d}_{31} & \bar{d}_{32} & 0 & 0 & 0 \end{bmatrix} \begin{Bmatrix} \varepsilon_{xx} \\ \varepsilon_{yy} \\ \gamma_{xy} \\ \gamma_{yz} \\ \gamma_{xz} \end{Bmatrix} + \frac{1}{2} \begin{bmatrix} a_{11} & 0 & 0 \\ 0 & a_{22} & 0 \\ 0 & 0 & \bar{a}_{33} \end{bmatrix} \begin{Bmatrix} E_x \\ E_y \\ E_z \end{Bmatrix} - \frac{1}{2} \begin{bmatrix} b_{11} & 0 & 0 \\ 0 & b_{22} & 0 \\ 0 & 0 & \bar{b}_{33} \end{bmatrix} \begin{Bmatrix} \kappa_x \\ \kappa_y \\ \kappa_z \end{Bmatrix}, \tag{2.43}$$

where c_{ij} and $\bar{c}_{ij}$ are the elastic and reduced elastic coefficients of the microplate, respectively, and $\bar{c}_{ij} = c_{ij} - (c_{i3}c_{j3}/c_{33})$ $(i, j = 1, 2)$. e_{ij} and $\bar{e}_{ij}$ are the piezoelectric and reduced piezoelectric coefficients of the microplate, respectively, and $\bar{e}_{3k} = e_{3k} - (e_{33}c_{k3}/c_{33})$ $(k = 1, 2)$. The variables d_{ij} and $\bar{d}_{ij}$ are the coupling force-stress and couple-stress coefficients and the reduced coupling force-stress and couple-stress coefficients of the microplate, respectively, and $\bar{d}_{3k} = d_{3k} - (d_{33}c_{k3}/c_{33})$ $(k = 1, 2)$. For an isotropic piezoelectric material, $\bar{c}_{11} = \bar{c}_{22} = E/(1-\upsilon^2)$, $\bar{c}_{12} = \upsilon E/(1-\upsilon^2)$, and $c_{44} = c_{55} = c_{66} = G = E/[2(1+\upsilon)]$, in which E and υ denote Young's modulus and Poisson's ratio, respectively, $e_{24} = e_{15} = d_{24} = d_{15} = 0$, $\bar{e}_{31} = \bar{e}_{32}$, $\bar{d}_{31} = \bar{d}_{32}$, and $\bar{b}_{31} = \bar{b}_{32}$. In addition, for an isotropic piezoelectric material, the coupling force-stress and couple-stress coefficients d_{ij} were deduced as being equal to zero by Hadjesfandiari [55]. The effect of d_{ij} has not been considered in the published literature so far, and so it has been discarded from the following derivation. Furthermore, η_{kk} and $\bar{\eta}_{kk}$ are the permittivity (or dielectric) and reduced permittivity (or dielectric) coefficients, respectively, and $\bar{\eta}_{33} = \eta_{33} + (e_{33}e_{33}/c_{33})$. For an isotropic piezoelectric material, the nonzero dielectric coefficients η_{11}, η_{22}, and η_{33} are defined as $\eta_{11} = \eta_{22} = \eta_{33} = \eta_e$. The variables a_{kk} and $\bar{a}_{kk}$ are the flexoelectric and reduced flexoelectric coefficients, respectively, and $\bar{a}_{33} = a_{33} - (e_{33}d_{33}/c_{33})$. For an isotropic piezoelectric material, the nonzero flexoelectric coefficients a_{11}, a_{22}, and a_{33} are defined following Hadjesfandiari [55] as $a_{11} = a_{22} = a_{33} = 4f_e$, where f_e denotes the flexoelectric parameter. The variables b_{kk} and $\bar{b}_{kk}$ are the coupling and reduced coupling coefficients between the couple-stress tensor and the skew-symmetric part of the curvature tensor,

respectively, and $\bar{b}_{33} = b_{33} - (d_{33}d_{33}/c_{33})$. For an isotropic piezoelectric material, the nonzero coupling coefficients between the couple-stress tensor and the skew-symmetric part of the curvature tensor b_{11}, b_{22}, and b_{33} are defined following HADJESFANDIARI [55] as $b_{11} = b_{22} = b_{33} = 16Gl^2$, where l represents the material length scale parameter. This parameter reflects the effect of the couple stress tensor which is significant when the dimensions of the structures are in the microscale and the nanoscale ranges.

2.3. Euler–Lagrange equations and the possible boundary conditions

Basing on Hamilton's principle, we derive the Euler–Lagrange equations associated with the possible boundary conditions for the unified size-dependent theory by requiring the first-order variation of the relevant energy functional in a time interval from t_1 to t_2 to be zero as follows:

$$\delta \int_{t_1}^{t_2} (T - U_s + W)\, dt = 0, \tag{2.44}$$

where T represents the kinetic energy functional, U_s denotes the strain energy functional, and W is the work done due to both the initial in-plane force resultants induced by the applied voltages acting on the top and bottom surfaces of the microplate and the restoring forces of the Winkler–Pasternak foundation. The variable $t$is the time, and the operator δ is called the variational operator.

The first-order variation of the kinetic energy functional can be written as

$$\begin{aligned}
\delta \int_{t_1}^{t_2} T\, dt = \int_{t_1}^{t_2} \Big\{ \iint_{\Omega} \Big[& - I_0 u_{,tt}\, \delta u - I_1 u_{,xtt}\, \delta w - I_3 u_{,tt}\, \delta\gamma_x + I_1 w_{,xtt}\, \delta u \\
& + I_2 w_{,xxtt}\, \delta w + I_4 w_{,xtt}\, \delta\gamma_x - I_3 \gamma_{x,tt}\, \delta u - I_4 \gamma_{x,xtt}\, \delta w \\
& - I_5 \gamma_{x,tt}\, \delta\gamma_x - I_0 v_{,tt}\, \delta v - I_1 v_{,ytt}\, \delta w - I_3 v_{,tt}\, \delta\gamma_y + I_1 w_{,ytt}\, \delta v \\
& + I_2 w_{,yytt}\, \delta w + I_4 w_{,ytt}\, \delta\gamma_y - I_3 \gamma_{y,tt}\, \delta v - I_4 \gamma_{y,ytt}\, \delta w \Big] \\
& - I_5 \gamma_{y,tt}\, \delta\gamma_y - I_0 w_{,tt}\, \delta w \Big\}\, d\Omega\, dt \\
& + \int_{t_1}^{t_2} \oint_{\Gamma} \Big\{ I_1 (u_{,tt}\, n_x + v_{,tt}\, n_y) \delta w - I_2 (w_{,xtt}\, n_x + w_{,ytt}\, n_y) \delta w \\
& + I_4 (\gamma_{x,tt}\, n_x + \gamma_{y,tt}\, n_y) \delta w \Big\}\, d\Gamma\, dt,
\end{aligned} \tag{2.45}$$

where Ω and Γ denote the mid-plane domain of the plate and its boundary edges, respectively; $(\, I_0 \;\, I_1 \;\, I_2 \;\, I_3 \;\, I_4 \;\, I_5 \,) = \int_{-h/2}^{h/2} \rho(\, 1 \;\, z \;\, z^2 \;\, f \;\, zf \;\, f^2 \,)\, dz$, and ρ denotes the mass density of the plate.

The first-order variation of the strain energy functional in the time interval $[t_1,\, t_2]$ can be written as

$$
\begin{aligned}
(2.46)\quad \delta \int_{t_1}^{t_2} U_s\, dt = \int_{t_1}^{t_2} \iint_{\Omega} \int_{-h/2}^{h/2} \Big[& \sigma_{(xx)}\delta\varepsilon_{xx} + \sigma_{(yy)}\delta\varepsilon_{yy} + \sigma_{(xy)}\delta\gamma_{xy} + \sigma_{(xz)}\delta\gamma_{xz} \\
& + \sigma_{(yz)}\delta\gamma_{yz} - 2\mu_{xy}\delta\kappa_{xy} - 2\mu_{yz}\delta\kappa_{yz} - 2\mu_{xz}\delta\kappa_{xz} \\
& - D_x\delta E_x - D_y\delta E_y - D_z\delta E_z \Big]\, d\Omega\, dz\, dt \\
= \int_{t_1}^{t_2} \iint_{\Omega} \Big\{ & N^{\sigma}_{(xx)}\delta u_{,x} - M^{\sigma}_{(xx)}\delta w_{,xx} + P^{\sigma}_{(xx)}\delta\gamma_{x,x} + N^{\sigma}_{(yy)}\delta v_{,y} \\
& - M^{\sigma}_{(yy)}\delta w_{,yy} + P^{\sigma}_{(yy)}\delta\gamma_{y,y} + N^{\sigma}_{(xy)}(\delta u_{,y} + \delta v_{,x}) \\
& - 2M^{\sigma}_{(xy)}\delta w_{,xy} + P^{\sigma}_{(xy)}(\delta\gamma_{x,y} + \delta\gamma_{y,x}) + R^{\sigma}_{(xz)}\delta\gamma_x + R^{\sigma}_{(yz)}\delta\gamma_y \\
& - M^{\mu}_{[xy]}(\delta w_{,xx} + \delta w_{,yy}) + \tfrac{1}{2} S^{\mu}_{[xy]}(\delta\gamma_{x,x} + \delta\gamma_{y,y}) \\
& - \tfrac{1}{2} M^{\mu}_{[yz]}(\delta u_{,yy} - \delta v_{,xy}) - \tfrac{1}{2} R^{\mu}_{[yz]}(\delta\gamma_{x,yy} - \delta\gamma_{y,xy}) - \tfrac{1}{2} T^{\mu}_{[yz]}\delta\gamma_x \\
& - \tfrac{1}{2} M^{\mu}_{[xz]}(\delta u_{,xy} - \delta v_{,xx}) - \tfrac{1}{2} R^{\mu}_{[xz]}(\delta\gamma_{x,xy} - \delta\gamma_{y,xx}) + \tfrac{1}{2} T^{\mu}_{[xz]}\delta\gamma_y \\
& - R^{D}_{x}\delta\phi_{,x} - R^{D}_{y}\delta\phi_{,y} - T^{D}_{z}\delta\phi \Big\}\, d\Omega\, dt,
\end{aligned}
$$

where the relationships between the relevant generalized force and moment resultants and the generalized displacement components are given in Appendix A.

By performing the integration by parts, we can rewrite Eq. (2.46) as follows:

$$
\begin{aligned}
(2.47)\quad \delta \int_{t_1}^{t_2} U_s\, dt = \int_{t_1}^{t_2} \iint_{\Omega} \Big\{ & - N^{\sigma}_{(xx),x}\,\delta u - M^{\sigma}_{(xx),xx}\,\delta w - P^{\sigma}_{(xx),x}\,\delta\gamma_x \\
& - N^{\sigma}_{(yy),y}\,\delta v - M^{\sigma}_{(yy),yy}\,\delta w - P^{\sigma}_{(yy),y}\,\delta\gamma_y - N^{\sigma}_{(xy),y}\,\delta u - N^{\sigma}_{(xy),x}\,\delta v \\
& - 2M^{\sigma}_{(xy),xy}\,\delta w - P^{\sigma}_{(xy),y}\,\delta\gamma_x - P^{\sigma}_{(xy),x}\,\delta\gamma_y + R^{\sigma}_{(xz)}\delta\gamma_x + R^{\sigma}_{(yz)}\delta\gamma_y \\
& - M^{\mu}_{[xy],xx}\,\delta w - M^{\mu}_{[xy],yy}\,\delta w - \tfrac{1}{2}[S^{\mu}_{[xy],x}\,\delta\gamma_x + S^{\mu}_{[xy],y}\,\delta\gamma_y] \\
& - \tfrac{1}{2}[M^{\mu}_{[yz],yy}\,\delta u - M^{\mu}_{[yz],xy}\,\delta v] - \tfrac{1}{2}[R^{\mu}_{[yz],yy}\,\delta\gamma_x - R^{\mu}_{[yz],xy}\,\delta\gamma_y] - \tfrac{1}{2} T^{\mu}_{[yz]}\delta\gamma_x \\
& - \tfrac{1}{2}[M^{\mu}_{[xz],xy}\,\delta u - M^{\mu}_{[xz],xx}\,\delta v] - \tfrac{1}{2}[R^{\mu}_{[xz],xy}\,\delta\gamma_x - R^{\mu}_{[xz],xx}\,\delta\gamma_y] \\
& + \tfrac{1}{2} T^{\mu}_{[xz]}\delta\gamma_y + R^{D}_{x},_{x}\,\delta\phi + R^{D}_{y},_{y}\,\delta\phi - T^{D}_{z}\delta\phi \Big\}\, d\Omega\, dt \\
& + \text{boundary condition terms.}
\end{aligned}
$$

The first-order variation of the work done is given as

$$\begin{aligned}(2.48)\qquad \delta\int_{t_1}^{t_2} W\,dt &= -\int_{t_1}^{t_2}\iint_{\Omega}(\bar{N}_{(xx)}\delta\varepsilon_{xx}^{nl}+\bar{N}_{(yy)}\delta\varepsilon_{yy}^{nl})\,d\Omega\,dt\\ &\quad -\int_{t_1}^{t_2}\iint_{\Omega}[k_w w-k_G(w_{,xx}+w_{,yy})]\delta w\,d\Omega\,dt\\ &\quad -\int_{t_1}^{t_2}\oint_{\Gamma}(k_G w_{,x}\,n_x+k_G w_{,y}\,n_y)\delta w\,d\Gamma\,dt\\ &= \int_{t_1}^{t_2}\iint_{\Omega}(\bar{N}_{(xx)}w_{,xx}+\bar{N}_{(yy)}w_{,yy})\delta w\,d\Omega\,dt\\ &\quad -\int_{t_1}^{t_2}\oint_{\Gamma}[\bar{N}_{(xx)}w_{,x}\,n_x+\bar{N}_{(yy)}w_{,y}\,n_y]\delta w\,d\Gamma\,dt\\ &\quad -\int_{t_1}^{t_2}\iint_{\Omega}[k_w w-k_G(w_{,xx}+w_{,yy})]\delta w\,d\Omega\,dt\\ &\quad -\int_{t_1}^{t_2}\oint_{\Gamma}(k_G w_{,x}\,n_x+k_G w_{,y}\,n_y)\delta w\,d\Gamma\,dt,\end{aligned}$$

where $\bar{N}_{(xx)}$ and $\bar{N}_{(yy)}$ are the initial in-plane force resultants induced by the applied voltages acting on the top and bottom surfaces of the microplate, and ε_{xx}^{nl} and ε_{yy}^{nl} are the von Kármán nonlinear strains. The variables of $\bar{N}_{(xx)}$, $\bar{N}_{(yy)}$, ε_{xx}^{nl}, and ε_{yy}^{nl} are given as follows:

$$(2.49)\qquad \bar{N}_{(xx)} = \int_{-h/2}^{h/2} e_{31}(2V_0/h)\,dz,$$

$$(2.50)\qquad \bar{N}_{(yy)} = \int_{-h/2}^{h/2} e_{32}(2V_0/h)\,dz,$$

$$(2.51)\qquad \varepsilon_{xx}^{nl} = \tfrac{1}{2}(w_{,x})^2,$$

$$(2.52)\qquad \varepsilon_{yy}^{nl} = \tfrac{1}{2}(w_{,y})^2,$$

where the initial in-plane force resultants, $\bar{N}_{(xx)}$ and $\bar{N}_{(yy)}$, induced in the piezoelectric plates which were formed by PZT-4 and PZT-5H are compressive as the applied voltages, V_0, are positive because their values of e_{31} and e_{32} are negative, and vice versa.

By substituting Eqs. (2.45), (2.47), and (2.48) into Eq. (2.44) and setting the coefficients of δu, δv, δw, $\delta\gamma_x$, $\delta\gamma_y$ and $\delta\phi$ to zero, we obtain the following Euler–Lagrange equations of the unified size-dependent piezoelectric plate theory and its associated possible boundary conditions:

$$\begin{aligned}
(2.53)\qquad \delta u:\ & -(N^{\sigma}_{(xx)}),_x -(N^{\sigma}_{(xy)}),_y -\tfrac{1}{2}(M^{\mu}_{[yz]}),_{yy} -\tfrac{1}{2}(M^{\mu}_{[xz]}),_{xy} \\
& = -I_0 u,_{tt} + I_1 w,_{xtt} - I_3 \gamma_x,_{tt}\,, \\
(2.54)\qquad \delta v:\ & -(N^{\sigma}_{(xy)}),_x -(N^{\sigma}_{(yy)}),_y +\tfrac{1}{2}(M^{\mu}_{[yz]}),_{xy} +\tfrac{1}{2}(M^{\mu}_{[xz]}),_{xx} \\
& = -I_0 v,_{tt} + I_1 w,_{ytt} - I_3 \gamma_y,_{tt}\,, \\
(2.55)\qquad \delta w:\ & -(M^{\sigma}_{(xx)}),_{xx} -2(M^{\sigma}_{(xy)}),_{xy} -(M^{\sigma}_{(yy)}),_{yy} -(M^{\mu}_{[xy]}),_{xx} \\
& -(M^{\mu}_{[xy]}),_{yy} -\bar{N}_{(xx)} w,_{xx} -\bar{N}_{(yy)} w,_{yy} +[k_w w - k_G(w,_{xx} + w,_{yy})] \\
& = -I_1 u,_{xtt} - I_1 v,_{ytt} + I_2 w,_{xxtt} + I_2 w,_{yytt} \\
& - I_4 \gamma_x,_{xtt} - I_4 \gamma_y,_{ytt} - I_0 w,_{tt}\,, \\
(2.56)\qquad \delta\gamma_x:\ & -(P^{\sigma}_{(xx)}),_x -(P^{\sigma}_{(xy)}),_y +(R^{\sigma}_{(xz)}) - \tfrac{1}{2}(S^{\mu}_{[xy]}),_x \\
& -\tfrac{1}{2}(R^{\mu}_{[xz]}),_{xy} -\tfrac{1}{2}(R^{\mu}_{[yz]}),_{yy} -\tfrac{1}{2}(T^{\mu}_{[yz]}) \\
& = -I_3 u,_{tt} + I_4 w,_{xtt} - I_5 \gamma_x,_{tt}\,, \\
\delta\gamma_y:\ & -(P^{\sigma}_{(xy)}),_x -(P^{\sigma}_{(yy)}),_y +(R^{\sigma}_{(yz)}) - \tfrac{1}{2}(S^{\mu}_{[xy]}),_y +\tfrac{1}{2}(R^{\mu}_{[xz]}),_{xx} \\
(2.57)\qquad & + \tfrac{1}{2}(R^{\mu}_{[yz]}),_{xy} +\tfrac{1}{2}(T^{\mu}_{[xz]}) \\
& = -I_3 v,_{tt} + I_4 w,_{ytt} - I_5 \gamma_y,_{tt}\,, \\
(2.58)\qquad \delta\phi:\ & (R^{D}_{x}),_x +(R^{D}_{y}),_y - T^{D}_{z} = 0.
\end{aligned}$$

The possible boundary conditions at the edges are obtained as follows:

$$\begin{aligned}
(2.59a)\qquad & \text{either } (N^{\sigma}_{(xx)})n_x + (N^{\sigma}_{(xy)})n_y + \tfrac{1}{2}(M^{\mu}_{[xz]}),_y\, n_x + \tfrac{1}{2}(M^{\mu}_{[yz]}),_y\, n_y = 0 \\
& \text{or } u = \hat{u}, \\
(2.59b)\qquad & \text{either } -\tfrac{1}{2}(M^{\mu}_{[xz]})n_y = 0 \text{ or } u,_x = \hat{u},_x\,, \\
(2.59c)\qquad & \text{either } -\tfrac{1}{2}(M^{\mu}_{[yz]})n_y = 0 \text{ or } u,_y = \hat{u},_y\,;
\end{aligned}$$

$$\begin{aligned}
(2.60a)\qquad & \text{either } (N^{\sigma}_{(xy)})n_x + (N^{\sigma}_{(yy)})n_y - \tfrac{1}{2}(M^{\mu}_{[xz]}),_x\, n_x - \tfrac{1}{2}(M^{\mu}_{[yz]}),_x\, n_y = 0 \\
& \text{or } v = \hat{v}, \\
(2.60b)\qquad & \text{either } \tfrac{1}{2}(M^{\mu}_{[xz]})n_x = 0 \text{ or } v,_x = \hat{v},_x\,,
\end{aligned}$$

(2.60c) either $\frac{1}{2}(M^{\mu}_{[yz]})n_x = 0$ or $v_{,y} = \hat{v}_{,y}$;

(2.61a) either $(M^{\sigma}_{(xx)})_{,x}\, n_x + (M^{\sigma}_{(yy)})_{,y}\, n_y + (M^{\sigma}_{(xy)})_{,x}\, n_y + (M^{\sigma}_{(xy)})_{,y}\, n_x$
$+ (M^{\mu}_{[xy]})_{,x}\, n_x + (M^{\mu}_{[xy]})_{,y}\, n_y + (\bar{N}_{(xx)} w_{,x}\, n_x + \bar{N}_{(yy)} w_{,y}\, n_y)$
$+ k_G(w_{,x}\, n_x + w_{,y}\, n_y) - I_1(u_{,tt}\, n_x + v_{,tt}\, n_y)$
$+ I_2(w_{,xtt}\, n_x + w_{,ytt}\, n_y) - I_4(\gamma_{x,tt}\, n_x + \gamma_{y,tt}\, n_y) = 0$
or $w = \hat{w}$,

(2.61b) either $-(M^{\sigma}_{(xx)})n_x - (M^{\sigma}_{(xy)})n_y - (M^{\mu}_{[xy]})n_x = 0$ or $w_{,x} = \hat{w}_{,x}$,

(2.61c) either $-(M^{\sigma}_{(xy)})n_x - (M^{\sigma}_{(yy)})n_y - (M^{\mu}_{[xy]})n_y = 0$ or $w_{,y} = \hat{w}_{,y}$;

(2.62a) either $(P^{\sigma}_{(xx)})n_x + (P^{\sigma}_{(xy)})n_y + \frac{1}{2}(S^{\mu}_{[xy]})n_x + \frac{1}{2}(R^{\mu}_{[xz]})_{,y}\, n_x$
$+ \frac{1}{2}(R^{\mu}_{[yz]})_{,y}\, n_y = 0$ or $\gamma_x = \hat{\gamma}_x$,

(2.62b) either $-\frac{1}{2}(R^{\mu}_{[xz]})n_y = 0$ or $\gamma_{x,x} = \hat{\gamma}_{x,x}$,

(2.62c) either $-\frac{1}{2}(R^{\mu}_{[yz]})n_y = 0$ or $\gamma_{x,y} = \hat{\gamma}_{x,y}$;

(2.63a) either $(P^{\sigma}_{(xy)})n_x + (P^{\sigma}_{(yy)})n_y + \frac{1}{2}(S^{\mu}_{[xy]})n_y$
$- \frac{1}{2}(R^{\mu}_{[xz]})_{,x}\, n_x - \frac{1}{2}(R^{\mu}_{[yz]})_{,x}\, n_y = 0$ or $\gamma_y = \hat{\gamma}_y$,

(2.63b) either $\frac{1}{2}(R^{\mu}_{[xz]})n_x = 0$ or $\gamma_{y,x} = \hat{\gamma}_{y,x}$,

(2.63c) either $\frac{1}{2}(R^{\mu}_{[yz]})n_x = 0$ or $\gamma_{y,y} = \hat{\gamma}_{y,y}$;

(2.64) either $-R^D_x n_x - R^D_y n_y = 0$ or $\phi = \hat{\phi}$,

where $\hat{u}$, $\hat{v}$, $\hat{w}$, $\hat{\gamma}_x$, $\hat{\gamma}_y$, and $\hat{\phi}$ represent the prescribed generalized displacement components along the edges of the microplate.

The following Euler–Lagrange equations expressed in terms of the generalized displacement components can be obtained by substituting Eqs. (A.1)–(A.21) into Eqs. (2.53)–(2.58):

(2.65) δu: $K_{11}u + K_{12}v + K_{13}w + K_{14}\gamma_x + K_{15}\gamma_y + K_{16}\phi$
$= -I_0 u_{,tt} + I_1 w_{,xtt} - I_3 \gamma_{x,tt}$,

(2.66) δv: $K_{21}u + K_{22}v + K_{23}w + K_{24}\gamma_x + K_{25}\gamma_y + K_{26}\phi$
$= -I_0 v_{,tt} + I_1 w_{,ytt} - I_3 \gamma_{y,tt}$,

(2.67) δw: $K_{31}u + K_{32}v + K_{33}w + K_{34}\gamma_x + K_{35}\gamma_y + K_{36}\phi$
$= -I_1 u_{,xtt} - I_1 v_{,ytt} - I_0 w_{,tt} + I_2(w_{,xxtt} + w_{,yytt})$
$- I_4(\gamma_{x,xtt} + \gamma_{y,ytt})$,

$$\delta\gamma_x\colon\ K_{41}u + K_{42}v + K_{43}w + K_{44}\gamma_x + K_{45}\gamma_y + K_{46}\phi = -I_3u_{,tt} + I_4w_{,xtt} - I_5\gamma_{x,tt}\,, \tag{2.68}$$

$$\delta\gamma_y\colon\ K_{51}u + K_{52}v + K_{53}w + K_{54}\gamma_x + K_{55}\gamma_y + K_{56}\phi = -I_3v_{,tt} + I_4w_{,ytt} - I_5\gamma_{y,tt}\,, \tag{2.69}$$

$$\delta\phi\colon\ K_{61}u + K_{62}v + K_{63}w + K_{64}\gamma_x + K_{65}\gamma_y + K_{66}\phi = -F^{\eta}_{33f}(V_0/h), \tag{2.70}$$

where

$$\begin{aligned}
K_{11} &= -(A_{11}\partial_{xx} + A_{66}\partial_{yy}) + \tfrac{1}{16}(A^b_{22}\partial_{xxyy} + A^b_{11}\partial_{yyyy}),\\
K_{12} &= -(A_{12} + A_{66})\partial_{xy} - \tfrac{1}{16}(A^b_{22}\partial_{xxxy} + A^b_{11}\partial_{xyyy}),\\
K_{13} &= B_{11}\partial_{xxx} + (B_{12} + 2B_{66})\partial_{xyy},\\
K_{14} &= -(A_{11f}\partial_{xx} + A_{66f}\partial_{yy}) + \tfrac{1}{16}(A^b_{22f}\partial_{xxyy} + A^b_{11f}\partial_{yyyy} + F^b_{11f}\partial_{yy}),\\
K_{15} &= -(A_{12f} + A_{66f})\partial_{xy} - \tfrac{1}{16}(A^b_{22f}\partial_{xxxy} + A^b_{11f}\partial_{xyyy} + F^b_{22f}\partial_{xy}),\\
K_{16} &= \hat{F}^e_{31f}\partial_x + \tfrac{1}{4}(\hat{E}^a_{11f} - \hat{E}^a_{22f})\partial_{xyy},\\
K_{21} &= K_{12},\\
K_{22} &= -(A_{66}\partial_{xx} + A_{22}\partial_{yy}) + \tfrac{1}{16}(A^b_{22}\partial_{xxxx} + A^b_{11}\partial_{xxyy}),\\
K_{23} &= (B_{12} + 2B_{66})\partial_{xxy} + B_{22}\partial_{yyy},\\
K_{24} &= -(A_{12f} + A_{66f})\partial_{xy} - \tfrac{1}{16}(A^b_{22f}\partial_{xxxy} + A^b_{11f}\partial_{xyyy} + F^b_{11f}\partial_{xy}),\\
K_{25} &= -(A_{66f}\partial_{xx} + A_{22f}\partial_{yy}) + \tfrac{1}{16}(A^b_{22f}\partial_{xxxx} + A^b_{11f}\partial_{xxyy} + F^b_{22f}\partial_{xx}),\\
K_{26} &= \hat{F}^e_{32f}\partial_y + \tfrac{1}{4}(\hat{E}^a_{22f} - \hat{E}^a_{11f})\partial_{xxy},\\
K_{31} &= -K_{13}, \quad K_{32} = -K_{23},\\
K_{33} &= [D_{11}\partial_{xxxx} + (2D_{12} + 4D_{66})\partial_{xxyy} + D_{22}\partial_{yyyy}] - [\bar{N}_{(xx)}\partial_{xx} + \bar{N}_{(yy)}\partial_{yy}]\\
&\quad + [k_w - k_G(\partial_{xx} + \partial_{yy})] + (A^b_{33}/4)[(\partial_{xxxx} + 2\partial_{xxyy} + \partial_{yyyy})],\\
K_{34} &= -[B_{11f}\partial_{xxx} + (B_{12f} + 2B_{66f})\partial_{xyy}] - (E^b_{33f}/8)(\partial_{xxx} + \partial_{xyy}),\\
K_{35} &= -[(B_{12f} + 2B_{66f})\partial_{xxy} + B_{22f}\partial_{yyy}] - (E^b_{33f}/8)(\partial_{xxy} + \partial_{yyy}),\\
K_{36} &= \hat{P}^e_{31f}\partial_{xx} + \hat{P}^e_{32f}\partial_{yy} + (\hat{F}^a_{33f}/2)(\partial_{xx} + \partial_{yy}),\\
K_{41} &= K_{14}, \quad K_{42} = K_{24}, \quad K_{43} = -K_{34},\\
K_{44} &= -(H_{11f}\partial_{xx} + H_{66f}\partial_{yy} - J_{55f}) + (1/16)[H^b_{22f}\partial_{xxyy} + H^b_{11f}\partial_{yyyy}\\
&\quad - J^b_{33f}\partial_{xx} + 2L^b_{11f}\partial_{yy} + N^b_{11f}],\\
K_{45} &= -(H_{12f} + H_{66f})\partial_{xy}\\
&\quad - \tfrac{1}{16}[H^b_{22f}\partial_{xxxy} + H^b_{11f}\partial_{xyyy} + (J^b_{33f} + L^b_{11f} + L^b_{22f})\partial_{xy}],\\
K_{46} &= (\hat{L}^e_{31f} - \bar{J}^e_{15f})\partial_x + (1/4)[(\hat{K}^a_{11f} - \hat{K}^a_{22f})\partial_{xyy} + (\hat{M}^a_{11f} + \bar{M}^a_{33f})\partial_x],\\
K_{51} &= K_{15}, \quad K_{52} = K_{25}, \quad K_{53} = -K_{35}, \quad K_{54} = K_{45},
\end{aligned}$$

$$
\begin{aligned}
K_{55} = & -(H_{66f}\partial_{xx} + H_{22f}\partial_{yy} - J_{44f}) + \tfrac{1}{16}[H^b_{22f}\partial_{xxxx} + H^b_{11f}\partial_{xxyy} \\
& + 2L^b_{22f}\partial_{xx} - J^b_{33f}\partial_{yy} + N^b_{22f}], \\
K_{56} = & (1/4)(\hat{K}^a_{22f} - \hat{K}^a_{11f})\partial_{xxy} + [(\hat{L}^e_{32f} - \bar{J}^e_{24f}) + \tfrac{1}{4}(\hat{M}^a_{22f} + \bar{M}^a_{33f})]\partial_y, \\
K_{61} = & -K_{16}, \quad K_{62} = -K_{26}, \quad K_{63} = K_{36}, \quad K_{64} = -K_{46}, \quad K_{65} = -K_{56}, \\
K_{66} = & \hat{J}^\eta_{11f}\partial_{xx} + \hat{J}^\eta_{22f}\partial_{yy} - \hat{N}^\eta_{33f},
\end{aligned}
$$

where the definitions of the coefficients

$$
(\, A_{ij}\ B_{ij}\ D_{ij}\ A_{ijf}\ B_{ijf}\ D_{ijf}\ E_{ijf}\ F_{ijf}\ H_{ijf}\ J_{ijf}\,),
$$

$$
(\, A^l_{ij}\ B^l_{ij}\ D^l_{ij}\ A^l_{ijf}\ B^l_{ijf}\ D^l_{ijf}\ E^l_{ijf}\ F^l_{ijf}\ H^l_{ijf}\ J^l_{ijf}\ K^l_{ijf}\ L^l_{ijf}\ M^l_{ijf}\ N^l_{ijf}\ P^l_{ijf}\,)
$$

($l = a$, b, and e), and

$$
(\, \hat{E}^l_{ijf}\ \hat{F}^l_{ijf}\ \hat{J}^l_{ijf}\ \bar{J}^l_{ijf}\ \hat{K}^l_{ijf}\ \hat{L}^l_{ijf}\ \hat{M}^l_{ijf}\ \bar{M}^l_{ijf}\ \hat{N}^l_{ijf}\ \hat{P}^l_{ijf}\,)
$$

($l = a$, b, and e) are given in Eqs. (A.25)–(A.27) presented in Appendix A.

3. Applications

Equations (2.65)–(2.70), which are associated with a set of boundary conditions presented in Eqs. (2.59a)–(2.64) can be formulated as a well-posed boundary value problem, for which the Navier-type analytical solutions of the natural frequencies for the free vibration analysis of a simply-supported, porous FG piezoelectric microplate can be obtained using the double Fourier series expansion method.

The simply-supported boundary conditions of such a microplate are expressed as follows:

At $x = 0$ and $x = L_x$,

$$N^\sigma_{(xx)} = 0, \tag{3.1}$$

$$v = 0, \tag{3.2}$$

$$w = 0, \tag{3.3}$$

$$M^\sigma_{(xx)} + M^\mu_{[xy]} = 0, \tag{3.4}$$

$$w_{,y} = 0, \tag{3.5}$$

$$P^\sigma_{(xx)} + \tfrac{1}{2}(S^\mu_{[xy]}) = 0, \tag{3.6}$$

$$\gamma_y = 0, \tag{3.7}$$

$$\phi = 0, \tag{3.8}$$

$$M^\mu_{[xz]} = M^\mu_{[yz]} = R^\mu_{[xz]} = R^\mu_{[yz]} = 0. \tag{3.9}$$

At $y = 0$ and $y = L_y$,

$$u = 0, \tag{3.10}$$

$$N^{\sigma}_{(yy)} = 0, \tag{3.11}$$

$$w = 0, \tag{3.12}$$

$$w_{,x} = 0, \tag{3.13}$$

$$M^{\sigma}_{(yy)} + M^{\mu}_{[xy]} = 0, \tag{3.14}$$

$$\gamma_x = 0, \tag{3.15}$$

$$P^{\sigma}_{(yy)} + \tfrac{1}{2} S^{\mu}_{[xy]} = 0, \tag{3.16}$$

$$\phi = 0, \tag{3.17}$$

$$M^{\mu}_{[xz]} = M^{\mu}_{[yz]} = R^{\mu}_{[xz]} = R^{\mu}_{[yz]} = 0. \tag{3.18}$$

By satisfying the simply-supported boundary conditions presented in Eqs. (3.1)–(3.18), we expand various field variables of the microplate as the double Fourier series as follows:

$$u = \sum_{\hat{m}=1}^{\infty} \sum_{\hat{n}=1}^{\infty} u_{\hat{m}\hat{n}} \cos(\tilde{m}x) \sin(\tilde{n}y) e^{i\omega t}, \tag{3.19}$$

$$v = \sum_{\hat{m}=1}^{\infty} \sum_{\hat{n}=1}^{\infty} v_{\hat{m}\hat{n}} \sin(\tilde{m}x) \cos(\tilde{n}y) e^{i\omega t}, \tag{3.20}$$

$$w = \sum_{\hat{m}=1}^{\infty} \sum_{\hat{n}=1}^{\infty} w_{\hat{m}\hat{n}} \sin(\tilde{m}x) \sin(\tilde{n}y) e^{i\omega t}, \tag{3.21}$$

$$\gamma_x = \sum_{\hat{m}=1}^{\infty} \sum_{\hat{n}=1}^{\infty} \gamma_{x\hat{m}\hat{n}} \cos(\tilde{m}x) \sin(\tilde{n}y) e^{i\omega t}, \tag{3.22}$$

$$\gamma_y = \sum_{\hat{m}=1}^{\infty} \sum_{\hat{n}=1}^{\infty} \gamma_{y\hat{m}\hat{n}} \sin(\tilde{m}x) \cos(\tilde{n}y) e^{i\omega t}, \tag{3.23}$$

$$\phi = \sum_{\hat{m}=1}^{\infty} \sum_{\hat{n}=1}^{\infty} \phi_{\hat{m}\hat{n}} \sin(\tilde{m}x) \sin(\tilde{n}y) e^{i\omega t}, \tag{3.24}$$

where $\tilde{m} = \hat{m}\pi/L_x$, and $\tilde{n} = \hat{n}\pi/L_y$, with $\hat{m}$ and $\hat{n}$ representing the half-wave numbers, which are positive integers. The symbol ω represents the natural frequency of the microplate.

Substituting Eqs. (3.19)–(3.24) into Euler–Lagrange Eqs. (2.65)–(2.70) leads to the following system of equations applied to the free vibration analysis of the piezoelectric microplate:

$$
(3.25)\qquad \left\{ \begin{bmatrix} k_{11} & k_{12} & k_{13} & k_{14} & k_{15} & k_{16} \\ k_{21} & k_{22} & k_{23} & k_{24} & k_{25} & k_{26} \\ k_{31} & k_{32} & k_{33} & k_{34} & k_{35} & k_{36} \\ k_{41} & k_{42} & k_{43} & k_{44} & k_{45} & k_{46} \\ k_{51} & k_{52} & k_{53} & k_{54} & k_{55} & k_{56} \\ k_{61} & k_{62} & k_{63} & k_{64} & k_{65} & k_{66} \end{bmatrix} \right.
$$

$$
\left. -\omega^2 \begin{bmatrix} I_0 & 0 & -\tilde{m}I_1 & I_3 & 0 & 0 \\ 0 & I_0 & -\tilde{n}I_1 & 0 & I_3 & 0 \\ -\tilde{m}I_1 & -\tilde{n}I_1 & \left[I_0+(\tilde{m}^2+\tilde{n}^2)I_2\right] & -\tilde{m}I_4 & -\tilde{n}I_4 & 0 \\ I_3 & 0 & -\tilde{m}I_4 & I_5 & 0 & 0 \\ 0 & I_3 & -\tilde{n}I_4 & 0 & I_5 & 0 \\ 0 & 0 & 0 & 0 & 0 & 0 \end{bmatrix} \right\} \begin{Bmatrix} u_{\hat{m}\hat{n}} \\ v_{\hat{m}\hat{n}} \\ w_{\hat{m}\hat{n}} \\ \gamma_{x\hat{m}\hat{n}} \\ \gamma_{y\hat{m}\hat{n}} \\ \phi_{\hat{m}\hat{n}} \end{Bmatrix} = \begin{Bmatrix} 0 \\ 0 \\ 0 \\ 0 \\ 0 \\ 0 \end{Bmatrix},
$$

where

$$
\begin{aligned}
k_{11} &= \tilde{m}^2 A_{11} + \tilde{n}^2 A_{66} + \tfrac{1}{16}(\tilde{m}^2\tilde{n}^2 A^b_{22} + \tilde{n}^4 A^b_{11}),\\
k_{12} &= k_{21} = \tilde{m}\tilde{n}(A_{12}+A_{66}) - \tfrac{1}{16}(\tilde{m}^3\tilde{n}A^b_{22} + \tilde{m}\tilde{n}^3 A^b_{11}),\\
k_{13} &= k_{31} = -\tilde{m}^3 B_{11} - \tilde{m}\tilde{n}^2(B_{12}+2B_{66}),\\
k_{14} &= k_{41} = \tilde{m}^2 A_{11f} + \tilde{n}^2 A_{66f} + \tfrac{1}{16}(\tilde{m}^2\tilde{n}^2 A^b_{22f} + \tilde{n}^4 A^b_{11f} - \tilde{n}^2 F^b_{11f}),\\
k_{15} &= k_{51} = \tilde{m}\tilde{n}(A_{12f}+A_{66f}) - \tfrac{1}{16}(\tilde{m}^3\tilde{n}A^b_{22f} + \tilde{m}\tilde{n}^3 A^b_{11f} - \tilde{m}\tilde{n}F^b_{22f}),\\
k_{16} &= k_{61} = \tfrac{1}{4}\tilde{m}\tilde{n}^2(\hat{E}^a_{22f} - \hat{E}^a_{11f}) + \tilde{m}\hat{F}^e_{31f},\\
k_{22} &= \tilde{m}^2 A_{66} + \tilde{n}^2 A_{22} + \tfrac{1}{16}(\tilde{m}^4 A^b_{22} + \tilde{m}^2\tilde{n}^2 A^b_{11}),\\
k_{23} &= k_{32} = -\tilde{m}^2\tilde{n}(B_{12}+2B_{66}) - \tilde{n}^3 B_{22},\\
k_{24} &= k_{42} = \tilde{m}\tilde{n}(A_{12f}+A_{66f}) - \tfrac{1}{16}(\tilde{m}^3\tilde{n}A^b_{22f} + \tilde{m}\tilde{n}^3 A^b_{11f} - \tilde{m}\tilde{n}F^b_{11f}),\\
k_{25} &= k_{52} = \tilde{m}^2 A_{66f} + \tilde{n}^2 A_{22f} + \tfrac{1}{16}(\tilde{m}^4 A^b_{22f} + \tilde{m}^2\tilde{n}^2 A^b_{11f} - \tilde{m}^2 F^b_{22f}),\\
k_{26} &= k_{62} = \tfrac{1}{4}\tilde{m}^2\tilde{n}(\hat{E}^a_{11f} - \hat{E}^a_{22f}) + \tilde{n}\hat{F}^e_{32f},\\
k_{33} &= \tilde{m}^4 D_{11} + \tilde{m}^2\tilde{n}^2(2D_{12}+4D_{66}) + \tilde{n}^4 D_{22} + \tfrac{1}{4}(\tilde{m}^4 + 2\tilde{m}^2\tilde{n}^2 + \tilde{n}^4)A^b_{33}\\
&\quad + [\tilde{m}^2\bar{N}_{(xx)} + \tilde{n}^2\bar{N}_{(yy)}] + [k_w + (\tilde{m}^2+\tilde{n}^2)k_G],\\
k_{34} &= k_{43} = -\tilde{m}^3 B_{11f} - \tilde{m}\tilde{n}^2(B_{12f}+2B_{66f}) - \tfrac{1}{8}(\tilde{m}^3 + \tilde{m}\tilde{n}^2)E^b_{33f},\\
k_{35} &= k_{53} = -\tilde{m}^2\tilde{n}(B_{12f}+2B_{66f}) - \tilde{n}^3 B_{22f} - \tfrac{1}{8}(\tilde{m}^2\tilde{n} + \tilde{n}^3)E^b_{33f},\\
k_{36} &= k_{63} = -(\tilde{m}^2\hat{P}^e_{31f} + \tilde{n}^2\hat{P}^e_{32f}) - \tfrac{1}{2}(\tilde{m}^2+\tilde{n}^2)\hat{F}^a_{33f},\\
k_{44} &= \tilde{m}^2 H_{11f} + \tilde{n}^2 H_{66f} + J_{55f} + \tfrac{1}{16}(\tilde{m}^2\tilde{n}^2 H^b_{22f} + \tilde{n}^4 H^b_{11f}\\
&\quad + \tilde{m}^2 J^b_{33f} - 2\tilde{n}^2 L^b_{11f} + N^b_{11f}),\\
k_{45} &= k_{54} = \tilde{m}\tilde{n}(H_{12f}+H_{66f}) - \tfrac{1}{16}[\tilde{m}^3\tilde{n}H^b_{22f} + \tilde{m}\tilde{n}^3 H^b_{11f}\\
&\quad - \tilde{m}\tilde{n}(J^b_{33f} + L^b_{11f} + L^b_{22f})],
\end{aligned}
$$

$$
\begin{aligned}
k_{46} &= k_{64} = \tilde{m}(\hat{L}^e_{31f} - \bar{J}^e_{15f}) + \tfrac{1}{4}[-\tilde{m}\tilde{n}^2(\hat{K}^a_{11f} - \hat{K}^a_{22f}) + \tilde{m}(\hat{M}^a_{11f} + \bar{M}^a_{33f})],\\
k_{55} &= \tilde{m}^2 H_{66f} + \tilde{n}^2 H_{22f} + J_{44f} + \tfrac{1}{16}(\tilde{m}^4 H^b_{22f} + \tilde{m}^2\tilde{n}^2 H^b_{11f}\\
&\quad - 2\tilde{m}^2 L^b_{22f} + \tilde{n}^2 J^b_{33f} + N^b_{22f}),\\
k_{56} &= k_{65} = \tilde{n}(\hat{L}^e_{32f} - \bar{J}^e_{24f}) - \tfrac{1}{4}[\tilde{m}^2\tilde{n}(\hat{K}^a_{22f} - \hat{K}^a_{11f}) - \tilde{n}(\hat{M}^a_{22f} + \bar{M}^a_{33f})],\\
k_{66} &= -\tilde{m}^2 \hat{J}^\eta_{11f} - \tilde{n}^2 \hat{J}^\eta_{22f} - \hat{N}^\eta_{33f}.
\end{aligned}
$$

Equation (3.25) represents the system of equations of the various CCST-based SDPTs which we used to evaluate the free vibration behavior of a simply-supported, porous FG piezoelectric microplate which resting on an elastic medium is subjected to electric voltages. The plate theories under consideration are the CCST-based CPT, the CCST-based FSDPT, the CCST-based RSDPT, the CCST-based SSDPT, the CCST-based ESDPT, and the CCST-based HSDPT.

Equation (3.25) can be rewritten in the following matrix form:

$$
\left\{ \begin{bmatrix} \mathbf{K}_{11} & \mathbf{K}_{12} \\ \mathbf{K}_{21} & \mathbf{K}_{22} \end{bmatrix} - \omega^2 \begin{bmatrix} \mathbf{M}_{11} & \mathbf{0} \\ \mathbf{0} & \mathbf{0} \end{bmatrix} \right\} \begin{Bmatrix} \mathbf{X}_1 \\ \mathbf{X}_2 \end{Bmatrix} = \begin{Bmatrix} \mathbf{0} \\ \mathbf{0} \end{Bmatrix}, \tag{3.26}
$$

where

$$
\mathbf{K}_{11} = \begin{bmatrix} k_{11} & k_{12} & k_{13} & k_{14} & k_{15} \\ k_{21} & k_{22} & k_{23} & k_{24} & k_{25} \\ k_{31} & k_{32} & k_{33} & k_{34} & k_{35} \\ k_{41} & k_{42} & k_{43} & k_{44} & k_{45} \\ k_{51} & k_{52} & k_{53} & k_{54} & k_{55} \end{bmatrix}, \quad \mathbf{K}_{12} = \begin{bmatrix} k_{16} \\ k_{26} \\ k_{36} \\ k_{46} \\ k_{56} \end{bmatrix}, \quad \mathbf{K}_{21} = \begin{bmatrix} k_{61} & k_{62} & k_{63} & k_{64} & k_{65} \end{bmatrix},
$$

$$
\mathbf{K}_{22} = [k_{66}], \quad \mathbf{M}_{11} = \begin{bmatrix} I_0 & 0 & -\tilde{m}I_1 & I_3 & 0 \\ 0 & I_0 & -\tilde{n}I_1 & 0 & I_3 \\ -\tilde{m}I_1 & -\tilde{n}I_1 & \left[I_0 + (\tilde{m}^2 + \tilde{n}^2)I_2\right] & -\tilde{m}I_4 & -\tilde{n}I_4 \\ I_3 & 0 & -\tilde{m}I_4 & I_5 & 0 \\ 0 & I_3 & -\tilde{n}I_4 & 0 & I_5 \end{bmatrix},
$$

$$
\mathbf{X}_1 = \begin{Bmatrix} u_{\hat{m}\hat{n}} \\ v_{\hat{m}\hat{n}} \\ w_{\hat{m}\hat{n}} \\ \gamma_{x\hat{m}\hat{n}} \\ \gamma_{y\hat{m}\hat{n}} \end{Bmatrix}, \quad \mathbf{X}_2 = \{\phi_{\hat{m}\hat{n}}\}.
$$

After partitioning, we separate Eq. (3.26) into the following form:

$$
\left[(\mathbf{K}_{11} - \mathbf{K}_{12}\mathbf{K}_{22}^{-1}\mathbf{K}_{21}) - \omega^2 \mathbf{M}_{11}\right]\mathbf{X}_1 = \mathbf{0}, \tag{3.27}
$$

$$
\mathbf{X}_2 = -\mathbf{K}_{22}^{-1}\mathbf{K}_{21}\mathbf{X}_1. \tag{3.28}
$$

The natural frequencies of the porous FG piezoelectric microplate can be obtained by setting the determinant of the coefficient matrix represented by Eq. (3.27) to zero as follows:

$$\left|(\mathbf{K}_{11} - \mathbf{K}_{12}\mathbf{K}_{22}^{-1}\mathbf{K}_{21}) - \omega^2\mathbf{M}_{11}\right| = 0. \tag{3.29}$$

As a result, five natural frequencies are obtained for a pair of half-wave numbers with fixed values $(\hat{m}, \hat{n})$, among which, one corresponds to the flexural mode, two correspond to the extensional mode, and two corresponds to the shear mode.

4. Numerical examples

In this section, the various size-dependent SDPTs based on the CCST which are derived in the preceding section, are used to obtain the Navier-type analytical solutions for the natural frequencies of simply-supported, porous FG piezoelectric microplates which resting on the Winkler–Pasternak foundation are subjected to electric voltages acting on the top and bottom surfaces. Some numerical examples are presented in the following subsections.

4.1. Porous FG piezoelectric macroplates

The relevant published literature contains no benchmark solutions for the natural frequencies of simply-supported, porous FG piezoelectric microplates resting on an elastic medium and subjected to electric voltages. Therefore, we reduce the unified size-dependent theory based on the CCST for analyzing piezoelectric microplates to a unified theory based on CCM for analyzing piezoelectric macroplates by setting the material length scale parameter (l) to zero. Various CCM-based plate theories can be reproduced from the unified CCM-based plate theory, including the CPT, the FSDPT, the RSDPT, the SSDPT, the ESDPT, and the HSDPT, by incorporating specific functions of $f(z)$ expressed in Eqs. (2.7)–(2.12) into the formulation of the unified theory based on the CCM. BARATI *et al.* [62] developed a refined four-variable SDPT (RFV-SDPT) to perform an analysis of the coupled electro-mechanical vibration behavior of porous FG piezoelectric macroplates subjected to electric voltages, by which their solutions are used to assess the accuracy of the reproduced various CCM-based plate theories. The constituent materials of the piezoelectric macroplates are PZT-4 and PZT-5H piezoceramics, of which their material properties are presented in Table 1.

Tables 2 and 3 show comparisons of the solutions for the fundamental (i.e., absolute lowest) natural frequencies of simply-supported, perfect FG piezoelectric macroscale plates and porous FG piezoelectric macroscale plates of Types A-1

Table 1. The elastic, piezoelectric, dielectric, and flexoelectric coefficients, the mass density, and the material length scale parameter of the PZT-4 and PZT-5H materials.

Material properties	PZT-4 [62]	PZT-5H [62]
$c_{11} = c_{22}$ [GPa]	138.499	99.201
c_{12} [GPa]	77.371	54.016
$c_{13} = c_{23}$ [GPa]	73.643	50.778
c_{33} [GPa]	114.745	86.856
$c_{44} = c_{55}$ [GPa]	25.6	21.1
c_{66} [GPa]	30.6	22.6
$e_{31} = e_{32}$ [C · m^{-2}]	−5.2	−7.209
e_{33} [C · m^{-2}]	15.08	15.118
$e_{24} = e_{15}$ [C · m^{-2}]	12.72	12.322
$\eta_{11} = \eta_{22}$ [C^2 · m^{-2}N^{-1}]	1.306×10^{-9}	1.53×10^{-9}
η_{33} [C^2 · m^{-2} · N^{-1}]	1.115×10^{-9}	1.5×10^{-9}
f_e [C · m^{-1}]	2×10^{-5}	1×10^{-5}
ρ [kg · m^{-3}]	7600	7750
l for the CCST [m]	8.8×10^{-6}	8.8×10^{-6}
$\hat{l}$ for the MCST [m]	17.6×10^{-6}	17.6×10^{-6}

and A-2 for different values of the half-wave number pairs, $(\hat{m},\ \hat{n})$, obtained using various CCM-based plate theories and the RFV-SDPT [62]. The plates are composed of PZT-4 and PZT-5H, with the top surface being made entirely of PZT-4 and the bottom surface being made entirely of PZT-5H. The macroplate material in the direction of the thickness are assumed to obey a power–Law distribution of the volume fractions of the constituents, PZT-4 and PZT-5H, with the through-thickness distribution of the volume fraction of the porosity defined in Eqs. (2.37a), (2.37b), and (2.37c) for the porous piezoelectric plates of the Types A-1, A-2, and A-3, respectively, and the effective material properties defined in Eq. (2.38) based on the rule of mixtures. A nondimensional natural frequency parameter is defined following Barati *et al.* [62] as $\bar{\omega} = \omega(L_x^2/h)\sqrt{\rho_{\text{PZT}-4}/(c_{11})_{\text{PZT}-4}}$ for the purposes of comparison.

In Table 2, the effects of the length-to-thickness ratio (L_x/h) and the porosity parameter (ψ_0) on the fundamental natural frequencies are investigated, with an applied voltage of zero $(V_0 = 0)$; $L_x/h = 5, 10$ and 20; $L_x = L_y$; $h = 0.01\,\text{m}$; $\kappa_p = 5$; and $\psi_0 = 0, 0.1$ and 0.2. In Table 3, the effects of the material-property gradient index (κ_p) and the porosity parameter (ψ_0) on the fundamental natural frequencies are examined, with $L_x/h = 100$; $L_x = L_y$; $h = 0.01\,\text{m}$; $V_0 = -500\,\text{V}$, 0 V, and 500 V; $\kappa_p = 0, 1$ and 5; and $\psi_0 = 0, 0.1$ and 0.2.

It can be seen in Table 2 that the CPT fails to produce accurate solutions for the fundamental natural frequencies of the porous piezoelectric macroscale

Table 2. Comparisons of the solutions for the fundamental frequency parameters of simply-supported, perfect piezoelectric macroscale plates and porous FG piezoelectric macroscale plates of Types A-1 and A-2 obtained using the CPT, various SDPTs, and the RFV-SDPT, with considering the effects of the length-to-thickness ratio and the porosity volume fraction.

Porosity distributions	Theories	$\psi_0 = 0$ (Perfect)			$\psi_0 = 0.1$ (Porous)			$\psi_0 = 0.2$ (Porous)		
		$L_x/h = 5$	$L_x/h = 10$	$L_x/h = 20$	$L_x/h = 5$	$L_x/h = 10$	$L_x/h = 20$	$L_x/h = 5$	$L_x/h = 10$	$L_x/h = 20$
Type A-1	CPT	5.439006	5.598554	5.640335	5.42156(11.7%)	5.58074(3.6%)	5.62242(0.1%)	5.39962(11.9%)	5.55836(3.7%)	5.59992(1.0%)
	FSDPT	5.046307	5.468012	5.604872	5.02895(3.7%)	5.45021(1.1%)	5.58696(0.6%)	5.00722(3.8%)	5.42788(1.3%)	5.56447(0.4%)
	RSDPT	5.041180	5.465953	5.604278	5.02356(3.5%)	5.44801(1.1%)	5.58632(0.6%)	5.00107(3.7%)	5.42540(1.2%)	5.56376(0.4%)
	SSDPT	5.041511	5.466028	5.604295	5.02356(3.5%)	5.44801(1.1%)	5.58632(0.6%)	5.00107(3.7%)	5.42540(1.2%)	5.56376(0.4%)
	ESDPT	5.042922	5.466498	5.604424	5.02495(3.6%)	5.44847(1.1%)	5.58645(0.6%)	5.00243(3.7%)	5.42586(1.2%)	5.56388(0.4%)
	HSDPT	5.041200	5.465965	5.604282	5.02328(3.5%)	5.44796(1.1%)	5.58631(0.6%)	5.00083(3.7%)	5.42537(1.2%)	5.56375(0.4%)
	RFV-SDPT [62]	NA	NA	NA	4.85157	5.38837	5.61866	4.82437	5.35978	5.54376
Type A-2	CPT	5.439006	5.598554	5.640335	5.50227(12.5%)	5.66598(3.8%)	5.70888(0.9%)	5.57142(13.6%)	5.73983(4.1%)	5.78400(1.0%)
	FSDPT	5.046307	5.468012	5.604872	5.07845(3.9%)	5.52454(1.2%)	5.67040(0.2%)	5.11219(4.3%)	5.58588(1.4%)	5.74204(0.3%)
	RSDPT	5.041180	5.465953	5.604278	5.06403(3.6%)	5.51909(1.1%)	5.66885(0.2%)	5.08547(3.7%)	5.57586(1.2%)	5.73919(0.2%)
	SSDPT	5.041511	5.466028	5.604295	5.06361(3.6%)	5.51889(1.1%)	5.66879(0.2%)	5.08400(3.7%)	5.57527(1.2%)	5.73902(0.2%)
	ESDPT	5.042922	5.466498	5.604424	5.06437(3.6%)	5.51913(1.1%)	5.66885(0.2%)	5.08382(3.7%)	5.57517(1.2%)	5.73899(0.2%)
	HSDPT	5.041200	5.465965	5.604282	5.06412(3.6%)	5.51913(1.1%)	5.66886(0.2%)	5.08566(3.7%)	5.57593(1.2%)	5.73921(0.2%)
	RFV-SDPT [62]	NA	NA	NA	4.88874	5.45957	5.65771	4.90228	5.51144	5.72560

The number in the parentheses represents the relative errors between the solutions obtained using the CCST-based plate theories and those obtained using the RFV-SDPT [62].

Table 3. Comparisons of the solutions for the fundamental frequency parameters of simply-supported, perfect piezoelectric macroscale plates and porous FG piezoelectric macroscale plates of Types A-1 and A-2 obtained using the CPT, various SDPTs, and the RFV-SDPT, with considering the effects of the material-property gradient index and the porosity volume fraction.

Porosity distributions	Electric voltages, V_0	Theories	$\psi_0 = 0$ (Perfect)			$\psi_0 = 0.2$ (Porous)		
			$\kappa_p = 0.2$	$\kappa_p = 1$	$\kappa_p = 5$	$\kappa_p = 0.2$	$\kappa_p = 1$	$\kappa_p = 5$
Type A-1	−500 V	CPT	6.19358(0.19%)	5.99226(0.18%)	5.84711(0.13%)	6.24365(0.07%)	5.98907(0.03%)	5.80884(0.07%)
		FSDPT	6.19215(0.22%)	5.99086(0.20%)	5.84570(0.15%)	6.24221(0.09%)	5.98767(0.06%)	5.80743(0.04%)
		RSDPT	6.19215(0.22%)	5.99086(0.20%)	5.84568(0.15%)	6.24222(0.09%)	5.98767(0.06%)	5.80740(0.04%)
		SSDPT	6.19215(0.22%)	5.99086(0.20%)	5.84568(0.15%)	6.24222(0.09%)	5.98767(0.06%)	5.80740(0.04%)
		ESDPT	6.19215(0.22%)	5.99086(0.20%)	5.84568(0.15%)	6.24222(0.09%)	5.98768(0.06%)	5.80740(0.04%)
		HSDPT	6.19215(0.22%)	5.99086(0.20%)	5.84568(0.15%)	6.24222(0.09%)	5.98767(0.06%)	5.80740(0.04%)
		RFV-SDPT [62]	6.20555	6.00294	5.85444	6.24814	5.99103	5.80503
Type A-1	0 V	CPT	6.01827(0.20%)	5.80735(0.18%)	5.65387(0.13%)	6.07064(0.07%)	5.80405(0.03%)	5.61339(0.07%)
		FSDPT	6.01680(0.22%)	5.80591(0.21%)	5.65242(0.16%)	6.06916(0.10%)	5.80262(0.05%)	5.61193(0.04%)
		RSDPT	6.01680(0.22%)	5.80590(0.21%)	5.65239(0.16%)	6.06916(0.10%)	5.80261(0.05%)	5.61190(0.04%)
		SSDPT	6.01680(0.22%)	5.80590(0.21%)	5.65239(0.16%)	6.06917(0.10%)	5.80261(0.05%)	5.61190(0.04%)
		ESDPT	6.01680(0.22%)	5.80591(0.21%)	5.65240(0.16%)	6.06917(0.10%)	5.80262(0.05%)	5.61190(0.04%)
		HSDPT	6.01680(0.22%)	5.80590(0.21%)	5.65239(0.16%)	6.06916(0.10%)	5.80261(0.05%)	5.61190(0.04%)
		RFV-SDPT [62]	6.03027	5.81787	5.66120	6.07512	5.80571	5.60954
Type A-1	500 V	CPT	5.83770(0.21%)	5.61635(0.18%)	5.4538(0.13%)	5.89255(0.08%)	5.61294(0.02%)	5.41088(0.07%)
		FSDPT	5.83618(0.23%)	5.61486(0.21%)	5.45228(0.16%)	5.89103(0.10%)	5.61146(0.05%)	5.40937(0.04%)
		RSDPT	5.83618(0.23%)	5.61485(0.21%)	5.45226(0.16%)	5.89103(0.10%)	5.61145(0.05%)	5.40934(0.04%)
		SSDPT	5.83618(0.23%)	5.61485(0.21%)	5.45226(0.16%)	5.89103(0.10%)	5.61145(0.05%)	5.40934(0.04%)
		ESDPT	5.83619(0.23%)	5.61486(0.21%)	5.45226(0.16%)	5.89104(0.10%)	5.61146(0.05%)	5.40934(0.04%)
		HSDPT	5.83618(0.23%)	5.61485(0.21%)	5.45226(0.16%)	5.89103(0.10%)	5.61145(0.05%)	5.40934(0.04%)
		RFV-SDPT [62]	5.84974	5.62671	5.46113	5.89704	5.61429	5.40698
Type A-2	−500 V	CPT	6.19358(0.19%)	5.99226(0.18%)	5.84711(0.13%)	6.36697(0.16%)	6.14589(0.15%)	5.98727(0.07%)
		FSDPT	6.19215(0.22%)	5.99086(0.20%)	5.84570(0.15%)	6.36528(0.19%)	6.14424(0.17%)	5.98560(0.10%)
		RSDPT	6.19215(0.22%)	5.99086(0.20%)	5.84568(0.15%)	6.36521(0.19%)	6.14416(0.17%)	5.98548(0.10%)
		SSDPT	6.19215(0.22%)	5.99086(0.20%)	5.84568(0.15%)	6.36520(0.19%)	6.14416(0.17%)	5.98547(0.10%)
		ESDPT	6.19215(0.22%)	5.99086(0.20%)	5.84568(0.15%)	6.36520(0.19%)	6.14416(0.17%)	5.98547(0.10%)
		HSDPT	6.19215(0.22%)	5.99086(0.20%)	5.84568(0.15%)	6.36521(0.19%)	6.14416(0.17%)	5.98548(0.10%)
		RFV-SDPT [62]	6.20555	6.00294	5.85444	6.37713	6.15487	5.99172
Type A-2	0 V	CPT	6.01827(0.20%)	5.80735(0.18%)	5.65387(0.13%)	6.19694(0.16%)	5.96575(0.15%)	5.79832(0.08%)
		FSDPT	6.01680(0.22%)	5.80591(0.21%)	5.65242(0.16%)	6.19520(0.19%)	5.96404(0.18%)	5.79659(0.11%)
		RSDPT	6.01680(0.22%)	5.80590(0.21%)	5.65239(0.16%)	6.19513(0.19%)	5.96396(0.18%)	5.79647(0.11%)
		SSDPT	6.01680(0.22%)	5.80590(0.21%)	5.65239(0.16%)	6.19512(0.19%)	5.96396(0.18%)	5.79647(0.11%)
		ESDPT	6.01680(0.22%)	5.80591(0.21%)	5.65240(0.16%)	6.19513(0.19%)	5.96396(0.18%)	5.79647(0.11%)
		HSDPT	6.01680(0.22%)	5.80590(0.21%)	5.65239(0.16%)	6.19513(0.19%)	5.96396(0.18%)	5.79647(0.11%)
		RFV-SDPT [62]	6.03027	5.81787	5.66120	6.20715	5.97455	5.80282
Type A-2	500 V	CPT	5.83770(0.21%)	5.61635(0.18%)	5.45380(0.13%)	6.02211(0.17%)	5.77999(0.15%)	5.60301(0.08%)
		FSDPT	5.83618(0.23%)	5.61486(0.21%)	5.45228(0.16%)	6.02032(0.20%)	5.77823(0.18%)	5.60122(0.11%)
		RSDPT	5.83618(0.23%)	5.61485(0.21%)	5.45226(0.16%)	6.02025(0.20%)	5.77814(0.18%)	5.60109(0.12%)
		SSDPT	5.83618(0.23%)	5.61485(0.21%)	5.45226(0.16%)	6.02024(0.20%)	5.77814(0.18%)	5.60109(0.12%)
		ESDPT	5.83619(0.23%)	5.61486(0.21%)	5.45226(0.16%)	6.02024(0.20%)	5.77814(0.18%)	5.60108(0.12%)
		HSDPT	5.83618(0.23%)	5.61485(0.21%)	5.45226(0.16%)	6.02025(0.20%)	5.77815(0.18%)	5.60109(0.12%)
		RFV-SDPT [62]	5.84974	5.62671	5.46113	6.03238	5.78861	5.60756

The number in the parentheses represents the relative errors between the solutions obtained using the CCST-based plate theories and those obtained using the RFV-SDPT [62].

plates when the value of the L_x/h ratio is equal to or less than 10. The solutions obtained using the CPT are always greater than those obtained using various SDPTs. This is due to the fact that the effect of shear deformations is not considered by the CPT, which results in an increase in the overall stiffness of the porous FG piezoelectric plates, which in turn leads to overemphasizing their fundamental natural frequencies. For example, the relative error between the solutions for the fundamental natural frequencies obtained using the CPT and those obtained using the RFV-SDPT is 1.0%, 3.7%, and 11.9% when $L_x/h = 20$ (thin plates), $L_x/h = 10$ (moderately thick plates), and $L_x/h = 5$ (thick plates), respectively, in the case of Type A-1 porous FG piezoelectric plates, and 1.0%, 4.1%, and 13.7%, respectively, in the case of Type A-2 porous FG piezoelectric plates, with a porosity parameter of $\psi_0 = 0.2$. When compared with the results of the fundamental natural frequencies obtained using the RFV-SDPT, the CPT and various SDPTs can be arranged in the following descending order of accuracy from the most accurate to the least accurate: (RSDPT, SSDPT, ESDPT, HSDPT) > FSDPT > CPT. The results also show that the solutions for the fundamental natural frequencies of the porous piezoelectric macroscale plates obtained using the RSDPT, the SSDPT, the ESDPT, and the HSDPT are in excellent agreement with those obtained using the RFV-SDPT for thin plates ($L_x/h = 20$) and moderately thick plates ($L_x/h = 10$). The disparity between them increases as the thickness of the porous FG piezoelectric plates increases because the effect of the transverse normal strain is considered by the RFV-SDPT but not considered by the other models. This indicates that the thicker the plates are, the more significant the effect of the transverse normal strain on the fundamental natural frequencies is. For example, the relative error between the solutions for the fundamental natural frequencies obtained using the RSDPT and those obtained using the RFV-SDPT is 0.4%, 1.2%, and 3.7% when $L_x/h = 20, 10$ and 5, respectively, in the case of Type A-1 porous FG piezoelectric plates, and 0.3%, 1.2%, and 3.7%, respectively, in the case of Type A-2 porous FG piezoelectric plates, with a porosity parameter of $\psi_0 = 0.2$. In addition, the fundamental natural frequencies of the perfect FG piezoelectric plates, when $\psi_0 = 0$, are not always greater than those of the porous FG piezoelectric plates, when $\psi_0 \neq 0$. The disparity between the solutions for the fundamental natural frequencies of the perfect FG piezoelectric plates and those for the porous FG piezoelectric plates increases as the value of the porosity parameters increases. This is because a high value of the porosity parameter is associated with a low overall stiffness of the plate, which then vibrates at lower fundamental natural frequencies. On the other hand, when the value of the porosity parameter is high, the mass moments of inertias are low. This causes the plate to vibrate at higher fundamental natural frequencies. If the increase in the fundamental natural frequencies resulting from low mass moments of inertias is more signifi-

cant than their decrease caused by a high overall plate stiffness, the fundamental natural frequencies of porous FG piezoelectric plates are greater than those of perfect FG piezoelectric plates, and vice versa.

It can be seen in Table 3 that when a positive electric voltage, $|V_0|$, is applied to the top surface of the plate and a negative electric voltage, $-|V_0|$, is applied to its bottom surface, a set of in-plane stresses which are initially compressive is induced, leading to a decrease in the overall stiffness of the plate and in turn decreasing the fundamental natural frequencies. Conversely, when a negative electric voltage, $-|V_0|$, is applied to the top surface of the plate and a positive electric voltage, $|V_0|$, is applied to the bottom surface of the plate, a set of in-plane stresses which are initially tensional is induced, leading to an increase in the overall stiffness of the plate and in turn increasing the fundamental natural frequencies. Again, the results also show that in the cases of $L_x/h = 100$ (very thin plates), the solutions for the fundamental natural frequencies of the porous FG piezoelectric plates obtained using the CPT and the various SDPTs which were reproduced from the unified size-dependent plate theory developed in this study confirm very well with those obtained using the RFV-SDPT.

4.2. Porous FG elastic microplates

In this section, the CCST-based unified size-dependent theory for analyzing piezoelectric microplates is reduced to that for analyzing elastic microplates by setting the piezoelectric and flexoelectric coefficients to zero for the purpose comparison. Karamanli and Aydogdu [63] analyzed the free vibration characteristics of simply-supported, porous FG elastic microplates using a transverse shear and normal deformation plate theory (TSNDPT) based on the MCST. Their solutions for the fundamental natural frequencies are used to validate the accuracy of the reduced size-dependent SDPTs based on the CCST which are discussed in the preceding subsection and are applied in this subsection to the analysis of elastic microplates.

Table 4 presents a comparison of the solutions for the fundamental natural frequencies of simply-supported, Type A-3 porous FG elastic microplates obtained using both a number of size-dependent SDPTs based on the CCST and the size-dependent TSNDPT based on the MCST, with an examination of the effects of the length-to-thickness ratio, the material length scale parameter-to-thickness ratio, and the porosity gradient index on the fundamental natural frequencies. The microplates are composed of silicon carbide (SiC) (ceramic material) and aluminum (Al) (metal material). The top surface is made completely of SiC, and the bottom surface is made completely of Al. The microplate material in the direction of the thickness is assumed to obey a power–law distribution of the volume fractions of the constituents, with the through-thickness distribu-

Table 4. Comparisons of the solutions for the fundamental frequency parameter of simply-supported, Type A-3 porous FG elastic microplates obtained using various CCST-based SDPTs, and the MCST-based TSNDPT, with considering the effects of the length-to-thickness ratio, the material length scale parameter-to-thickness ratio, and the porosity gradient index ($L_x/h = 10$).

L_x/h	$\hat{l}/h(l/h)$	Theories	$\psi_0 = 0$			$\psi_0 = 0.05$			$\psi_0 = 0.1$		
			$\kappa_p = 1$	$\kappa_p = 2$	$\kappa_p = 5$	$\kappa_p = 1$	$\kappa_p = 2$	$\kappa_p = 5$	$\kappa_p = 1$	$\kappa_p = 2$	$\kappa_p = 5$
10	0 (0)	CCST-based RSDPT	4.09116(1.8%)	3.61803(2.9%)	3.31633(2.8%)	4.09385(1.8%)	3.61783(2.9%)	3.31633(2.8%)	4.09652(1.8%)	3.61762(2.8%)	3.31633(2.8%)
		CCST-based SSDPT	4.09124(1.8%)	3.61785(2.9%)	3.31525(2.8%)	4.09391(1.8%)	3.61763(2.9%)	3.31524(2.8%)	4.09657(1.8%)	3.61738(2.9%)	3.31523(2.8%)
		CCST-based ESDPT	4.09157(1.8%)	3.61793(2.9%)	3.31454(2.9%)	4.09423(1.8%)	3.61769(2.9%)	3.31453(2.9%)	4.09688(1.8%)	3.61742(2.9%)	3.31451(2.9%)
		CCST-based HSDPT	4.09117(1.8%)	3.61806(2.9%)	3.31645(2.8%)	4.09385(1.8%)	3.61786(2.9%)	3.31645(2.8%)	4.09653(1.8%)	3.61763(2.8%)	3.31644(2.8%)
		MCST-based TSNDPT [63]	4.1667	3.7243	3.4122	4.1689	3.724	3.4122	4.1711	3.7237	3.4122
10	0.4 (0.2)	CCST-based RSDPT	5.66842(0.8%)	4.99640(1.4%)	4.39583(1.4%)	5.67383(0.2%)	4.99587(1.2%)	4.39570(1.4%)	5.67924(0.4%)	4.99528(1.0%)	4.39557(1.4%)
		CCST-based SSDPT	5.66875(0.8%)	4.99606(1.4%)	4.39388(1.4%)	5.67415(0.2%)	4.99550(1.2%)	4.39375(1.4%)	5.67953(0.4%)	4.99490(1.0%)	4.39362(1.4%)
		CCST-based ESDPT	5.66991(0.8%)	4.99651(1.4%)	4.39287(1.5%)	5.67528(0.2%)	4.99593(1.2%)	4.39273(1.5%)	5.68064(0.4%)	4.99532(1.0%)	4.39260(1.5%)
		CCST-based HSDPT	5.66843(0.8%)	4.99647(1.4%)	4.39604(1.4%)	5.67384(0.2%)	4.99594(1.2%)	4.39592(1.4%)	5.67925(0.4%)	4.99536(1.0%)	4.39579(1.4%)
		MCST-based TSNDPT [63]	5.7137	5.0651	4.4585	5.6863	5.0563	4.4581	5.6593	5.0475	4.4577
10	0.8 (0.4)	CCST-based RSDPT	8.84891(0.1%)	7.78058(0.4%)	6.63537(0.4%)	8.85901(0.9%)	7.77934(0.1%)	6.63497(0.4%)	8.86910(1.8%)	7.77803(0.2%)	6.63456(0.4%)
		CCST-based SSDPT	8.84967(0.1%)	7.78022(0.4%)	6.63361(0.4%)	8.85974(0.9%)	7.77897(0.1%)	6.63321(0.4%)	8.86979(1.8%)	7.77765(0.2%)	6.63280(0.4%)'
		CCST-based ESDPT	8.85208(0.1%)	7.78122(0.3%)	6.63294(0.4%)	8.86211(0.9%)	7.77995(0.1%)	6.63254(0.4%)	8.87211(1.8%)	7.77862(0.2%)	6.63213(0.4%)
		CCST-based HSDPT	8.84892(0.1%)	7.78068(0.3%)	6.63558(0.4%)	8.85903(0.9%)	7.77943(0.1%)	6.63517(0.4%)	8.86912(1.8%)	7.77812(0.2%)	6.63477(0.4%)
		MCST-based TSNDPT [63]	8.858	7.808	6.661	8.7841	7.7855	6.6598	8.7112	7.7632	6.6586
10	1 (0.5)	CCST-based RSDPT	10.62669(0.1%)	9.33812(0.1%)	7.90579(0.1%)	10.52917(0.1%)	9.30844(0.1%)	7.90419(0.1%)	10.43278(0.0%)	9.27909(0.1%)	7.90260(0.1%)
		CCST-based SSDPT	10.62766(0.1%)	9.33777(0.1%)	7.90413(0.2%)	10.52999(0.1%)	9.30809(0.1%)	7.90254(0.2%)	10.43345(0.0%)	9.27873(0.1%)	7.90095(0.2%)
		CCST-based ESDPT	10.63069(0.1%)	9.33903(0.1%)	7.90363(0.2%)	10.53279(0.1%)	9.30931(0.1%)	7.90203(0.2%)	10.43604(0.1%)	9.27992(0.1%)	7.90045(0.2%)
		CCST-based HSDPT	10.62670(0.1%)	9.33822(0.1%)	7.90599(0.1%)	10.52920(0.1%)	9.30854(0.1%)	7.90439(0.1%)	10.43281(0.0%)	9.27920(0.1%)	7.90280(0.1%)
		MCST-based TSNDPT [63]	10.6204	9.3499	7.9174	10.5238	9.3205	7.9159	10.4283	9.2915	7.9143

[a] Symbols l and $\hat{l}$ represent the material length scale parameters defined in the CCST and MCST, respectively, and $l = \hat{l}/2$. In Table 4, the values of $\hat{l}$ and l are given following [56] to be $\hat{l} = 15\,\mu$m and $l = 7.5\,\mu$m, respectively.

[b] The number in the parentheses represents the relative errors between the solutions obtained using the CCST-based plate theories and those obtained using the TSNDPT [63].

tion of the material properties defined in Eq. (2.38) and the through-thickness distribution of the volume fraction of the porosity defined in Eq. (2.37c). The geometric parameters are set at $L_x/h = 10$; and $L_x = L_y$. The porosity parameter is assigned the values of $\psi_0 = 0, 0.05$ and 0.1. The material-property gradient index is considered as $\kappa_p = 1, 2$ and 5. The material properties of SiC and Al are given as follows:

For the SiC,

$$\begin{aligned} &E_{\mathrm{SiC}} = E_t = 427\,\mathrm{GPa}, \quad \upsilon_{\mathrm{SiC}} = \upsilon_t = 0.17, \\ &\rho_{\mathrm{SiC}} = \rho_t = 3100\,\mathrm{kg/m^3}, \quad \hat{l} = 2l = 15 \times 10^{-6}\,\mathrm{m}; \end{aligned} \tag{4.1a}$$

for the Al,

$$\begin{aligned} &E_{\mathrm{Al}} = E_b = 70\,\mathrm{GPa}, \quad \upsilon_{Al} = \upsilon_b = 0.3, \\ &\rho_{\mathrm{Al}} = \rho_b = 2702\,\mathrm{kg/m^3}, \quad \hat{l} = 2l = 15 \times 10^{-6}\,\mathrm{m}, \end{aligned} \tag{4.1b}$$

where $\hat{l}$ denotes the value of the material length scale parameter of the MCST. This value is two times that of the CCST because in the case of the former theory, the relationship between the symmetric couple stress tensor and the symmetric part of the curvature tensor was defined as $m_{ij} = 2G\hat{l}^2\chi_{ij}$ by Yang *et al.* [20], whereas in the latter theory, Hadjesfandiari and Dargush [53, 54] defined the relationship between the skew-symmetric couple stress tensor and the skew-symmetric part of the curvature tensor as $\mu_{ij} = -8Gl^2\kappa_{ij}$.

A nondimensional natural frequency parameter is defined as

$$\bar{\omega} = \omega(L_x^2/h)\sqrt{\rho_{\mathrm{SiC}}/E_{\mathrm{SiC}}}$$

following the work of Karamanli and Aydogdu [63] for the purposes of comparison.

It can be seen in Table 4 that the solutions for the fundamental natural frequencies of simply-supported, Type A-3 porous FG elastic microplates obtained using the reduced various size-dependent SDPTs (i.e., the CCST-based RSDPT, the CCST-based SSDPT, the CCST-based ESDPT, and the CCST-based HSDPT) are in excellent agreement with those obtained using the size-dependent MCST-based TSNDPT. The results also show that the fundamental natural frequencies increase as the $\hat{l}/h$ ratio increases and as the L_x/h ratio decreases, which indicates that both an increase in the value of the $\hat{l}/h$ ratio and a decrease in the value of the L_x/h ratio enhance the overall stiffness of the microplates, which in turn increases the fundamental natural frequency of its vibration.

4.3. Porous FG piezoelectric microplates

In this section, we conduct a parameter study to assess the significance of some key effects on the natural frequencies of simply-supported, porous FG

piezoelectric microplates of Types B-1, B-2, B-3, and B-4 which resting on the Winkler–Pasternak foundation are subjected to electric voltages acting on the top and bottom surfaces. The effects in questions include that of the material length scale parameter, the length-to-thickness ratio, the material-property gradient index, different values of the applied voltages, the porosity parameter, different porosity distribution patterns, the Winkler spring constant, and the shear modulus of the medium surrounding the microplate. The functions of the volume fractions of the porosity in the direction of the thickness for porous FG piezoelectric microplates of Types B-1, B-2, B-3, and B-4 are given in Eqs. (2.39a)–(2.39d), respectively, and their effective material properties are estimated using Eq. (2.40). In order to provide a clear picture of the variations in porosity for these four types of porous microplates, we present the non-dimensional volume fractions of the porosity in the direction of the thickness for each type in Fig. 2. It can be seen in Fig. 2 that the pores are uniformly distributed in the thickness direction of the microplate for Type B-1, and they concentrate around the mid-plane of the microplate for Type B-2; whereas, the pores concentrate around the bottom surface and around the top surface of the microplate for Type B-3 and Type B-4, respectively.

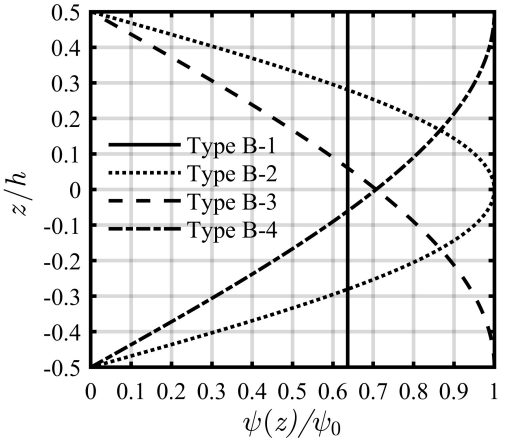

FIG. 2. The through-thickness distributions of the non-dimensional volume fraction of the porosity for porous piezoelectric microplates of Types B-1, B-2, B-3, and B-4.

Tables 5 and 6 show the lowest and the second lowest natural frequencies, respectively, of simply-supported, perfect FG piezoelectric microplates and Type A-2 porous FG piezoelectric microplates subjected to electric voltages obtained using the CCST-based RSDPT for the following specific values of half-wave number pairs: $(\hat{m}, \hat{n}) = (1,1), (1,2), (1,3), (2,2), (2,3)$ and $(3,3)$. The microplates are composed of PZT-4 and PZT-5H piezoelectric materials, with the top sur-

Table 5. The lowest frequency parameter solutions corresponding to the flexural vibration mode of simply-supported, perfect FG piezoelectric microplates and Type A-2 porous FG piezoelectric microplates obtained using the CCST-based RSDPT.

(l/h)	κ_p	Perfect or porous microplates	Electric voltages, V_0	$(\hat{m},\hat{n})=(1,1)$	$(\hat{m},\hat{n})=(1,2)$	$(\hat{m},\hat{n})=(1,3)$	$(\hat{m},\hat{n})=(2,2)$	$(\hat{m},\hat{n})=(2,3)$	$(\hat{m},\hat{n})=(3,3)$
0.4 (0.2)	1	Perfect ($\psi_0=0$)	−500 V	6.86994	16.06490	30.24729	24.71888	38.24418	50.92558
			0	6.50441	15.68595	29.85346	24.33068	37.84235	50.51123
			500 V	6.11708	15.29762	29.45433	23.93617	37.43616	50.09339
		Porous ($\psi_0=0.2$)	−500 V	6.97335	16.27229	30.52744	24.98141	38.52967	51.17978
			0	6.61378	15.89863	30.13744	24.59762	38.13081	50.76707
			500 V	6.23350	15.51597	29.74230	24.20773	37.72770	50.35090
	5	Perfect ($\psi_0=0$)	−500 V	6.68416	15.58329	29.28938	23.94907	37.00866	49.23867
			0	6.30064	15.18486	28.87456	23.54044	36.58506	48.80133
			500 V	5.89221	14.77567	28.45366	23.12456	36.15644	48.35996
		Porous ($\psi_0=0.2$)	−500 V	6.76919	15.74261	29.47244	24.13398	37.16820	49.31976
			0	6.39023	15.34783	29.05948	23.72792	36.74541	48.88160
			500 V	5.98733	14.94260	28.64052	23.31476	36.31765	48.43941
0.8 (0.4)	1	Perfect ($\psi_0=0$)	−500 V	9.26015	21.72287	41.20984	33.57909	52.31559	*70.07508
			0	8.71642	21.16256	40.63363	33.00881	51.73099	*69.47727
			500 V	8.13642	20.58698	40.04908	32.42847	51.13962	*68.87413
		Porous ($\psi_0=0.2$)	−500 V	9.33837	21.89821	41.49932	33.82849	52.65488	*70.47735
			0	8.79992	21.34343	40.92868	33.26378	52.07582	*69.88506
			500 V	8.22630	20.77382	40.34991	32.68928	51.49015	*69.28756
	5	Perfect ($\psi_0=0$)	−500 V	8.94586	20.92152	39.65065	32.31610	50.32570	*67.39695
			0	8.37091	20.32817	39.04031	31.71205	49.70648	*66.76378
			500 V	7.75344	19.71694	38.42020	31.09622	49.07934	*66.12439
		Porous ($\psi_0=0.2$)	−500 V	8.99185	21.01594	39.78503	32.43920	50.46838	*67.53711
			0	8.41932	20.42511	39.17713	31.83764	49.85153	*66.90622
			500 V	7.80490	19.81665	38.55957	31.22443	49.22684	*66.26916

[a]Symbols l and $\hat{l}$ represent the material length scale parameters defined in the CCST and MCST, respectively, and $l=\hat{l}/2$.
[b]The solutions with a superscript "$*$" represent the second lowest frequency parameter solutions of the piezoelectric microplates.

Table 6. The second lowest frequency parameter solutions corresponding to the extensional vibration mode of simply-supported, perfect FG piezoelectric microplates and Type A-2 porous FG piezoelectric microplates obtained using the CCST-based RSDPT.

(l/h)	κ_p	Perfect or porous microplates	Electric voltages, V_0	$(\hat{m},\hat{n})=(1,1)$	$(\hat{m},\hat{n})=(1,2)$	$(\hat{m},\hat{n})=(1,3)$	$(\hat{m},\hat{n})=(2,2)$	$(\hat{m},\hat{n})=(2,3)$	$(\hat{m},\hat{n})=(3,3)$
0.4 (0.2)	1	Perfect ($\psi_0=0$)	−500 V	19.43257	30.88392	44.04164	39.25349	50.45050	59.83916
			0 V	19.43257	30.88392	44.04164	39.25349	50.45050	59.83916
			500 V	19.43257	30.88392	44.04164	39.25349	50.45050	59.83916
		Porous ($\psi_0=0.2$)	−500 V	19.43149	30.87967	44.02980	39.24498	50.43316	59.81137
			0 V	19.43149	30.87967	44.02980	39.24498	50.43316	59.81137
			500 V	19.43149	30.87967	44.02980	39.24498	50.43316	59.81137
	5	Perfect ($\psi_0=0$)	−500 V	18.37914	29.21583	41.67897	37.14492	47.75937	56.67126
			0 V	18.37914	29.21583	41.67897	37.14492	47.75937	56.67126
			500 V	18.37914	29.21583	41.67897	37.14492	47.75937	56.67126
		Porous ($\psi_0=0.2$)	−500 V	18.10756	28.78381	41.06257	36.59644	47.05436	55.83572
			0 V	18.10756	28.78381	41.06257	36.59644	47.05436	55.83572
			500 V	18.10756	28.78381	41.06257	36.59644	47.05436	55.83572
0.8 (0.4)	1	Perfect ($\psi_0=0$)	−500 V	19.63191	31.66206	46.19899	40.80969	53.61213	*64.89588
			0 V	19.63191	31.66206	46.19899	40.80969	53.61213	*64.89588
			500 V	19.63191	31.66206	46.19899	40.80969	53.61213	*64.89588
		Porous ($\psi_0=0.2$)	−500 V	19.63057	31.65687	46.18487	40.79946	53.59169	*64.86369
			0 V	19.63057	31.65687	46.18487	40.79946	53.59169	*64.86369
			500 V	19.63057	31.65687	46.18487	40.79946	53.59169	*64.86369
	5	Perfect ($\psi_0=0$)	−500 V	18.57525	29.98099	43.79861	38.67429	50.86407	*61.63324
			0 V	18.57525	29.98099	43.79861	38.67429	50.86407	*61.63324
			500 V	18.57525	29.98099	43.79861	38.67429	50.86407	*61.63324
		Porous ($\psi_0=0.2$)	−500 V	18.30271	29.54518	43.17148	38.11809	50.14306	*60.77154
			0 V	18.30271	29.54518	43.17148	38.11809	50.14306	*60.77154
			500 V	18.30271	29.54518	43.17148	38.11809	50.14306	*60.77154

[a]Symbols l and $\hat{l}$ represent the material length scale parameters defined in the CCST and MCST, respectively, and $l=\hat{l}/2$.
[b]The solutions with a superscript "$*$" represent the lowest frequency parameter solutions of the piezoelectric microplates.

face composed entirely of PZT-4 and the bottom surface composed entirely of PZT-5H. The microplate material in the direction of the thickness is assumed to obey a power–law distribution of the volume fractions of the constituents, PZT-4 and PZT-5H. The through-thickness distribution of the material properties is defined in Eq. (2.38) and that of the volume fractions of the porosity is defined in Eq. (2.37b). The material properties of the PZT-4 and PZT-5H are presented in Table 1, in which a nondimensional natural frequency parameter is defined as $\bar{\omega} = \omega(L_x^2/h)\sqrt{\rho_{\text{PZT-4}}/(c_{11})_{\text{PZT-4}}}$.

The geometric parameters of the porous piezoelectric microplates are: $L_x/h = 10$, $L_x = L_y$, $\kappa_p = 1$ and 5, $\psi_0 = 0$ and 0.2. The values of the $\hat{l}/h$ ratio are $\hat{l}/h = 0.4$ and 0.8, where $\hat{l} = 17.6\,\mu\text{m}$ and $l = 8.8\,\mu\text{m}$. The pairs of the applied voltages are$V_0 = -500\,\text{V}$, $0\,\text{V}$ and $500\,\text{V}$.

Tables 5 and 6 show the solutions for the lowest and the second lowest natural frequencies, respectively, which correspond to the flexural and extensional vibration modes, respectively, of simply-supported, perfect FG piezoelectric microplates and Type A-2 porous FG piezoelectric microplates for different values of half-wave number pairs obtained using the CCST-based RSDPT. Again, it can be seen in these tables that both frequencies increase as the $\hat{l}/h$ ratio increases and as the value of κ_p decreases. When a positive electric voltage, $|V_0|$, is applied to the top surface of the microplate and a negative electric voltage, $-|V_0|$, is applied to its bottom surface, the lowest and second lowest natural frequencies decrease. Conversely, when a negative electric voltage, $-|V_0|$, is applied to the top surface of the plate and a positive electric voltage, $|V_0|$, is applied to its bottom surface, the lowest and the second lowest natural frequencies increase. It should be noted that the impacts of the material length scale parameter, the material-property gradient index, and the values of the applied voltages on the natural frequencies in the flexural vibration mode are much more significant than they are on the natural frequencies in the extensional vibration mode. The absolute lowest (fundamental) natural frequencies always occur when the half-wave number pair is $(\hat{m}, \hat{n}) = (1, 1)$. Some solutions show a superscript "$*$" for those of the half-wave number pair of $(\hat{m}, \hat{n}) = (3, 3)$, as shown in Tables 5 and 6, which means that the lowest natural frequencies correspond to the extensional vibration mode and the second lowest natural frequencies correspond to the flexural vibration mode, which is the exact opposite of the cases when $(\hat{m}, \hat{n}) \neq (3, 3)$.

Figure 3 shows the mode shapes for the flexural vibration modes, respectively, of the porous FG piezoelectric microplate in the xy-plane, for the following specific values of half-wave number pairs: $(\hat{m}, \hat{n}) = (1, 1), (1, 2), (1, 3), (2, 2), (2, 3)$, and $(3, 3)$, when $L_x/h = 10$, $L_x = L_y$, $\psi_0 = 0.25$, $\kappa_p = 2$, $V_0 = 0$ V, $\hat{l}/h = 0.4$ (i.e. $l/h = 0.2$), and $\hat{l} = 17.6 \times 10^{-6}$ m ($l = 8.8 \times 10^{-6}$ m).

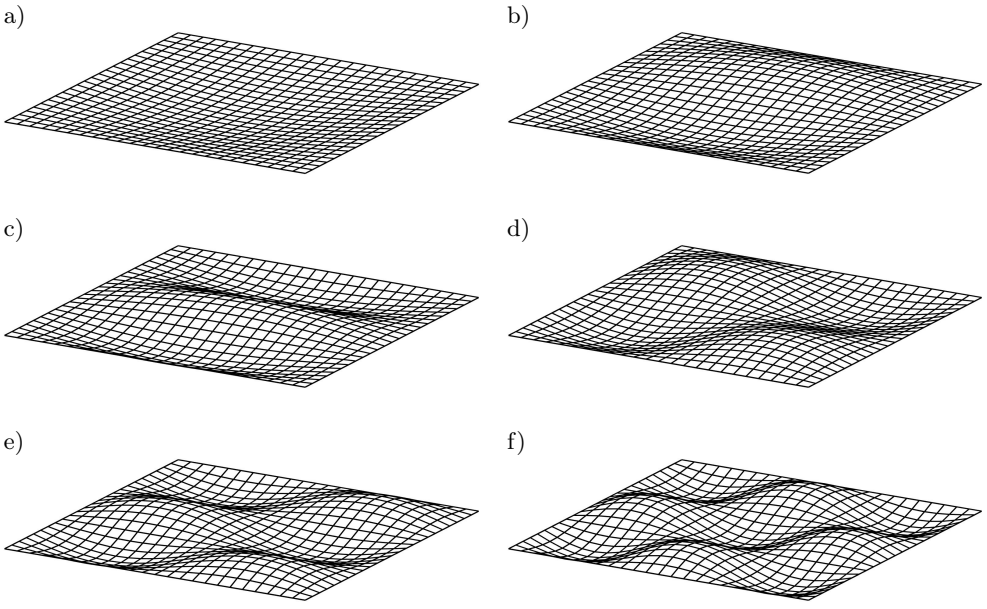

FIG. 3. Distributions of the modal deflection $u_z(x, y, 0)$ for the flexural vibration modes of the porous FG piezoelectric microplate in the xy-plane, with specific values of half-wave number pairs: a) $(\hat{m}, \hat{n}) = (1, 1)$, b) $(\hat{m}, \hat{n}) = (1, 2)$, c) $(\hat{m}, \hat{n}) = (1, 3)$, d) $(\hat{m}, \hat{n}) = (2, 2)$, e) $(\hat{m}, \hat{n}) = (2, 3)$, f) $(\hat{m}, \hat{n}) = (3, 3)$, where all of the displacements of each mode in each figure occur on the z axis.

Figure 4 shows the variations in the lowest natural frequencies of simply-supported, porous FG piezoelectric microplates of Types B-1, B-2, B-3, and B-4, with the values of applied voltages (V_0), when $L_x/h = 10$, $L_x = L_y$, V_0 varys from $-500\,\mathrm{V}$ to $500\,\mathrm{V}$, $\psi_0 = 0.5$, $\kappa_p = 2$, $l/h = 0$–0.5, and $l = 8.8 \times 10^{-6}$ m, and $(\hat{m}, \hat{n}) = (1, 1)$. It can be seen in Fig. 4 that the lowest natural frequencies of porous FG piezoelectric microplates decrease as the applied voltages V_0 increase. This is because when a pair of voltages, $|V_0|$ and $-|V_0|$, are applied to the top and bottom surfaces of the microplate, respectively, an initial state of compressive in-plane stress is induced, causing a decrease in the overall stiffness of the microplate which in turn decreases the lowest natural frequencies of its vibrations (see Eqs. (2.49) and (2.50)). In addition, when the applied voltages increase, the lowest natural frequencies become monotonically smaller, and their relationship approximates a linear function with a negative slope. For different types of porosity distributions, the impact of the porosity parameter on the lowest natural frequencies can be displayed in the following descending order from the most to the least significant: Type B-2 > Type B-1 > (Type B-3, Type B-4). This can be explained by the fact that when the porosity parameters of various

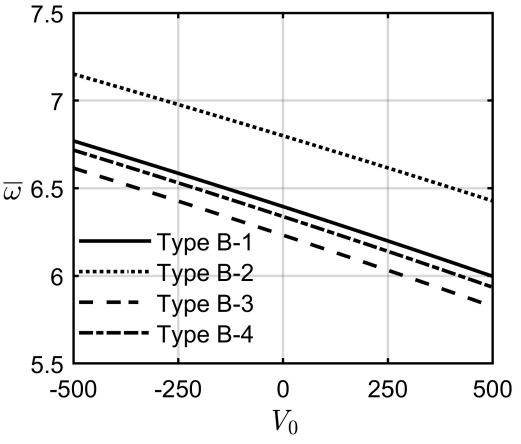

Fig. 4. Variations in the lowest natural frequencies of porous FG piezoelectric microplates of Types B-1, B-2, B-3, and B-4 with the applied voltages V_0 of different values.

porous microplates are the same, the more the pores are concentrated in the mid-plane of each microplate, which means that its mass is distributed farther away from its mid-plane, the higher its overall stiffness is, which in turn increases its lowest frequency parameters.

Figure 5 shows the variations in the lowest natural frequencies of simply-supported, porous FG piezoelectric microplates of Types B-1, B-2, B-3, and B-4, with the l/h ratio, when $L_x/h = 10$, $L_x = L_y$, $V_0 = 0$, $\psi_0 = 0.5$, $\kappa_p = 2$,

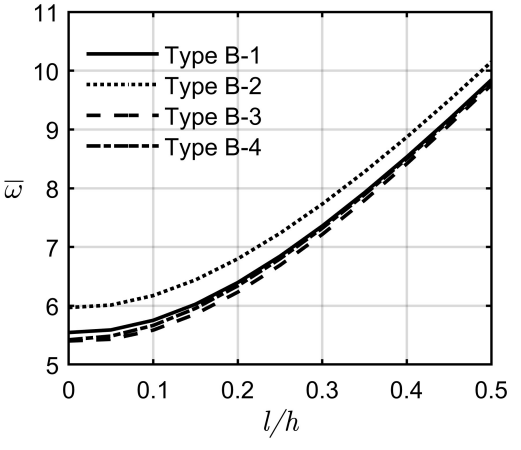

Fig. 5. Variations in the lowest natural frequencies of types B-1, B-2, B-3, and B-4 porous FG piezoelectric microplates with the l/h ratio.

$l/h = 0$–0.5, and $l = 8.8 \times 10^{-6}$ m, and $(\hat{m}, \hat{n}) = (1, 1)$. It can be seen in Fig. 5 that the lowest natural frequencies increase as the l/h ratio increases, which indicates that an increase in the material length scale parameter enhances the overall stiffness of the microplate, which in turn increases its lowest natural frequencies. Again, the lowest natural frequencies for porous piezoelectric microplates of Types B-1, B-2, B-3, B-4 are presented in descending order from the highest to the lowest value: Type B-2 > Type B-1 > (Type B-3, Type B-4).

Figure 6 shows that the lowest natural frequencies of simply-supported, porous FG piezoelectric microplates of Types B-1, B-2, B-3, and B-4 vary according to changes in the material-property gradient index κ_p, when $L_x/h = 10$, $L_x = L_y$, $V_0 = 0$, $\kappa_p = 0 - 10$, $l/h = 0.2$, $l = 8.8 \times 10^{-6}$ m, $\psi_0 = 0.5$, and $(\hat{m}, \hat{n}) = (1, 1)$. It can be seen in Fig. 6 that the lowest natural frequencies of a porous FG piezoelectric microplate decrease as the value of κ_p becomes greater. On the one hand, this indicates that an increase in the value of κ_p is associated with both an increase in the volume fraction of the softer material, PZT-5H and a decrease in that of the stiffer material, PZT-4, the result is a lower overall stiffness of the microplates. On the other hand, when an increase in the value of κ_p is linked to both an increase in the volume fraction of the heavier material, PZT-5H, and a decrease in that of the lighter material, PZT-4, the result is a higher overall mass moment of inertia of the microplates. Both a decrease in the overall stiffness of the microplate and an increase in the overall mass moment of inertia of the microplates cause a decrease in its lowest natural frequencies.

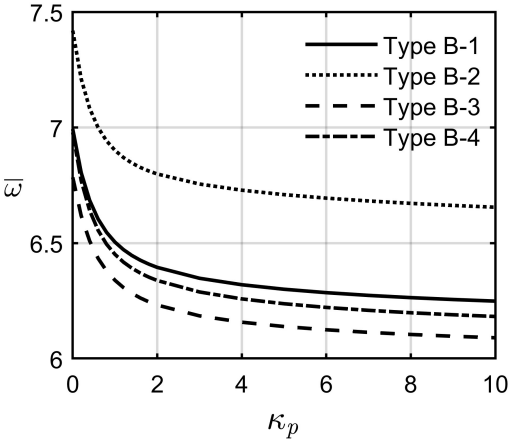

FIG. 6. Variations in the lowest natural frequencies of porous FG piezoelectric microplates of Types B-1, B-2, B-3, and B-4 with the material-property gradient index κ_p.

The lowest natural frequencies of simply-supported, Type B-2 FG porous piezoelectric microplates can be seen to vary in Fig. 7(a) according to the di-

mensionless Winkler stiffness K_W and in Fig. 7(b) according to the dimensionless shear modulus K_G of the medium surrounding the microplate, respectively, when $K_W = k_w E h^3/L_x^4$ and $K_G = k_G E h^3/L_x^2$. The relevant geometric and material parameters are $L_x = L_y$, $L_x/h = 10$ and 20, $l/h = 0.2$, $l = 8.8 \times 10^{-6}$ m, $V_0 = 0$, $\psi_0 = 0$ and 0.2, $\kappa_p = 2$, and $(\hat{m}, \hat{n}) = (1, 1)$. In Fig. 7(a), K_G is assigned the value of zero, and the values of K_W changes from 0 to 100. In Fig. 7(b), K_W is assigned to the value of 10, and the values of K_G changes from 0 to 10.

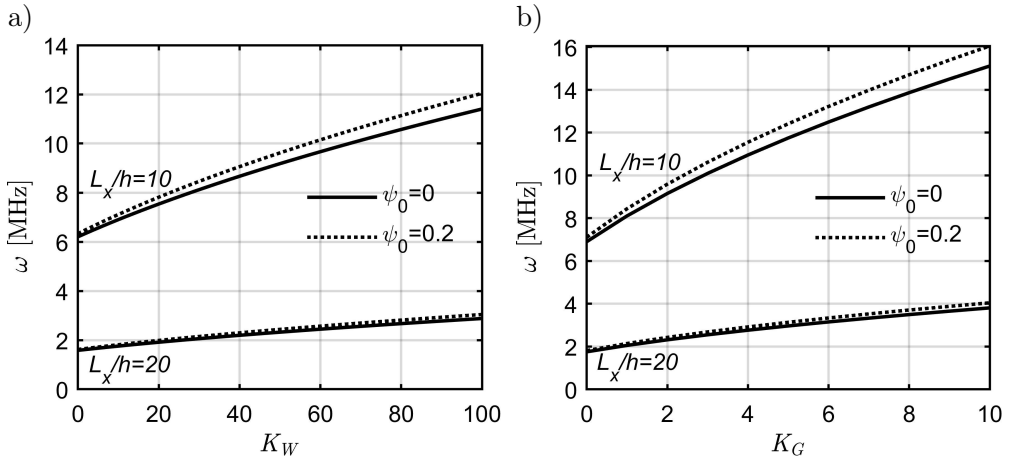

Fig. 7. Variations in the lowest natural frequencies of simply-supported, Type B-2 FG porous piezoelectric microplates with (a) the dimensionless Winkler stiffness K_W and (b) the dimensionless shear modulus K_G of the surrounding medium, respectively, when $K_W = k_w E h^3/L_x^4$ and $K_G = k_G E h^3/L_x^2$.

It can be seen in Fig. 7 that the lowest natural frequencies of simply-supported, porous FG piezoelectric microplates increase as the values of K_W and K_G increase, which indicates that the surrounding medium makes the microplates stiffer. The results show that the increase in K_W and K_G associated with the increase in the lowest frequencies when $L_x/h = 10$ is much higher than that occur when $L_x/h = 20$, which indicates that the interactive effect between the porous piezoelectric microplates and their surrounding medium is more significant for the thick plates than it is for thin plates. In addition, when the values of K_W and K_G increase by the same amount, the increase in the lowest natural frequencies for the latter is larger than it is for the former, which indicates that the impact of K_G on the lowest natural frequencies is more significant than that of K_W.

5. Concluding remarks

In this work, we developed a unified size-dependent theory based on the CCST for analyzing the free vibration behavior of porous FG piezoelectric microplates which resting on an elastic medium were subjected to electric voltages. Various CCST-based size-dependent SDPTs (i.e., the CCST-based CPT, FSDPT, RSDPT, SSDPT, ESDPT, and HSDPT) were reproduced by incorporating their corresponding shape functions characterizing the through-thickness distributions of shear deformations into our unified size-dependent theory. Euler–Lagrange equations and the possible boundary conditions for our unified CCST-based size-dependent theory were derived using Hamilton's principle. The Navier-type analytical solutions for the free vibration analysis of simply-supported, porous FG piezoelectric microplates were obtained and discussed in the numerical examples presented above.

The following are some conclusions that can be drawn from this study:

1. The unified size-dependent theory for analyzing porous piezoelectric microplates presented herein can be reduced to one unified size-dependent theory for analyzing porous piezoelectric macroplates and to another one for analyzing porous elastic microplates by setting the material length scale parameter to zero and by setting the piezoelectric and flexoelectric coefficients to zero, respectively.

2. Implementations of the unified size-dependent theory in the numerical examples, it was shown that the solutions obtained using the RSDPT, SSDPT, ESDPT, and HSDPT were in excellent agreement with the approximate 3D solutions obtained using the RFV-SDPT. For example, the relative error between the solutions for the frequency parameters obtained using various SDPTs mentioned above and those obtained using the RFV-SDPT was less than 1.2% in the cases of moderately thick plates ($L_x/h = 10$) and thin plates ($L_x/h = 20$), as well as it was less than 3.7% in the cases of thick plates ($L_x/h = 5$).

3. When the porosity parameters of various porous microplates were the same, the more the pores were concentrated in the mid-plane of each microplate, which means that its mass was distributed farther away from its mid-planes, the higher its overall stiffness was, which in turn increased its lowest natural frequencies. Therefore, the lowest natural frequencies of the various porous microplates considered in the numerical examples can be arranged in the following descending order from the highest to the lowest value: Type B-2 > Type B-1 > (Type B-3, Type B-4).

4. The results showed that the lowest natural frequencies of a porous FG piezoelectric microplate ($\psi_0 \neq 0$) were greater than those of a perfect FG piezoelectric microplate ($\psi_0 = 0$). On the one hand, this is because the increase in the value of the porosity parameter resulted in a decrease in the overall stiffness of the microplate, which in turn decreased the lowest natural frequencies. On the

other hand, the higher the value of the porosity parameter was, the lower the mass moments of inertia of the microplate were, which then led to an increase in the lowest natural frequencies. In cases where the increase in these frequencies resulting from a decrease in the mass moments of inertia was more significant than their decrease caused by the decrease in the microplate's overall stiffness, the lowest natural frequencies of the porous FG piezoelectric plates were greater than those of the perfect FG piezoelectric plates.

5. If a pair of voltages, $|V_0|$ and $-|V_0|$, were applied to the top and bottom surfaces of a microplate, respectively, an initial state of compressive in-plane stress was induced resulting in a decrease occurred in the microplate's overall stiffness, which then decreased the lowest natural frequencies. On the other hand, if a pair of voltages, $-|V_0|$ and $|V_0|$, were applied on the top and bottom surfaces of a microplate, respectively, an initial state of tensional in-plane stress was induced resulting in an increase in the microplate's overall stiffness, which then increased the lowest natural frequencies.

6. The lowest natural frequencies of a porous piezoelectric microplate decreased with the increase in the value of κ_p. This was the result of two factors. On the one hand, when an increase in the value of κ_p was associated with both an increase in the volume fraction of the softer material, PZT-5H, and a decrease in that of the stiffer material, PZT-4, the result was a lower overall stiffness of the microplate. On the other hand, when an increase in the value of κ_p was linked to both an increase in the volume fraction of the heavier material, PZT-5H, and a decrease in that of the lighter material, PZT-4, the result is a higher overall mass moment of inertia of the microplate. Both a decrease in the overall stiffness of the microplate and an increase in the overall mass moments of inertia of the microplate caused a decrease in the lowest natural frequencies.

7. The lowest natural frequencies of a simply-supported, porous FG piezoelectric microplate increased as the values of K_W and K_G became greater. The impact of the interactive effect between the microplate and its surrounding medium in the case of thick plates was more significant than it was in the case of thin plates, and the impact of K_G on the lowest frequencies was more significant than that of K_W.

The benefits of our unified size-dependent plate theory induce the fact that various size-dependent SDPTs based on the CCST were reproduced by incorporating their corresponding shape functions characterizing the through-thickness distributions of transverse shear deformations into this unified theory, which allows for comparisons of the results obtained using various size-dependent SDPTs to be made, and subsequent discussions of these results can be readily carried out. The implementation of the various CCST-based SDPTs examined in the numerical examples presented above showed that the CCST-based RSDPT, SSDPT, ESDPT, and HSDPT exhibited an excellent performance in terms of their

analyses of both moderately thick and thin porous piezoelectric microplates in cases where the plane stress assumptions were met and the parameters of most of the microplates used in MEMSs for practical applications fell within the scope of our unified size-dependent plate theory.

Future research could extend the range of uses for this unified size-dependent plate theory by applying it to the analysis of the mechanical behavior of various microscale shells of revolution, including cylindrical shells, doubly-curved shells, conical shells, spherical shells, toroidal shells. Follow-up research could replace the Cartesian coordinate system with their corresponding orthogonal curvilinear coordinate systems. In addition, the strong form-based analytical approach presented in this article is suitable for the application to simply-supported cases only. In order to extend the application of the unified size-dependent shear deformation plate theory to various boundary conditions, it is required to develop relevant weak form-based numerical methods, including the finite element method and the meshless method, which has been ongoing.

Appendix A: The relationships between the generalized force and moment resultants and the generalized displacement components

The relevant generalized force and moment resultants in Eqs. (2.49)–(2.54) can be expressed in terms of the generalized displacement components as follows:

$$
\begin{aligned}
(\mathrm{A.1}) \quad N^{\sigma}_{(xx)} &= \int_{-h/2}^{h/2} \sigma_{(xx)}\, dz \\
&= A_{11}u_{,x} + A_{12}v_{,y} - B_{11}w_{,xx} - B_{12}w_{,yy} + A_{11f}\gamma_{x,x} + A_{12f}\gamma_{y,y} \\
&\quad - \hat{F}^{e}_{31f}\phi + A^{e}_{31}(2V_0/h), \\
(\mathrm{A.2}) \quad N^{\sigma}_{(yy)} &= \int_{-h/2}^{h/2} \sigma_{(yy)}\, dz \\
&= A_{12}u_{,x} + A_{22}v_{,y} - B_{12}w_{,xx} - B_{22}w_{,yy} + A_{12f}\gamma_{x,x} + A_{22f}\gamma_{y,y} \\
&\quad - \hat{F}^{e}_{32f}\phi + A^{e}_{32}(2V^0/h), \\
(\mathrm{A.3}) \quad N^{\sigma}_{(xy)} &= \int_{-h/2}^{h/2} \tau_{(xy)}\, dz \\
&= A_{66}u_{,y} + A_{66}v_{,x} - 2B_{66}w_{,xy} + A_{66f}(\gamma_{x,y} + \gamma_{y,x}),
\end{aligned}
$$

$$(A.4)\quad M^{\sigma}_{(xx)} = \int_{-h/2}^{h/2} \sigma_{(xx)} z\, dz$$
$$= B_{11}u_{,x} + B_{12}v_{,y} - D_{11}w_{,xx} - D_{12}w_{,yy} + B_{11f}\gamma_{x,x} + B_{12f}\gamma_{y,y} - \hat{P}^{e}_{31f}\phi + B^{e}_{31}(2V_0/h),$$

$$(A.5)\quad M^{\sigma}_{(yy)} = \int_{-h/2}^{h/2} \sigma_{(yy)} z\, dz$$
$$= B_{12}u_{,x} + B_{22}v_{,y} - D_{12}w_{,xx} - D_{22}w_{,yy} + B_{12f}\gamma_{x,x} + B_{22f}\gamma_{y,y} - \hat{P}^{e}_{32f}\phi + B^{e}_{32}(2V_0/h),$$

$$(A.6)\quad M^{\sigma}_{(xy)} = \int_{-h/2}^{h/2} \sigma_{(xy)} z\, dz$$
$$= B_{66}u_{,y} + B_{66}v_{,x} - 2D_{66}w_{,xy} + B_{66f}(\gamma_{x,y} + \gamma_{y,x}),$$

$$(A.7)\quad Q^{\sigma}_{(xz)} = \int_{-h/2}^{h/2} \sigma_{(xz)}\, dz = E_{55f}\gamma_x - \hat{E}^{e}_{15f}\phi_{,x}\,,$$

$$(A.8)\quad Q^{\sigma}_{(yz)} = \int_{-h/2}^{h/2} \sigma_{(yz)}\, dz = E_{44f}\gamma_y - \hat{E}^{e}_{24f}\phi_{,y}\,,$$

$$(A.9)\quad P^{\sigma}_{(xx)} = \int_{-h/2}^{h/2} \sigma_{(xx)} f\, dz$$
$$= A_{11f}u_{,x} + A_{12f}v_{,y} - B_{11f}w_{,xx} - B_{12f}w_{,yy} + H_{11f}\gamma_{x,x} + H_{12f}\gamma_{y,y} - \hat{L}^{e}_{31f}\phi + A^{e}_{31f}(2V_0/h),$$

$$(A.10)\quad P^{\sigma}_{(yy)} = \int_{-h/2}^{h/2} \sigma_{(yy)} f\, dz$$
$$= A_{12f}u_{,x} + A_{22f}v_{,y} - B_{12f}w_{,xx} - B_{22f}w_{,yy} + H_{12f}\gamma_{x,x} + H_{22f}\gamma_{y,y} - \hat{L}^{e}_{32f}\phi + A^{e}_{32f}(2V_0/h),$$

$$(A.11)\quad P^{\sigma}_{(xy)} = \int_{-h/2}^{h/2} \sigma_{(xy)} f\, dz$$
$$= A_{66f}u_{,y} + A_{66f}v_{,x} - 2B_{66f}w_{,xy} + H_{66f}(\gamma_{x,y} + \gamma_{y,x}),$$

$$(A.12)\quad R^{\sigma}_{(xz)} = \int_{-h/2}^{h/2} \sigma_{(xz)}(Df)\,dz = J_{55f}\gamma_x - \bar{J}^{e}_{15f}\phi_{,x}\,,$$

$$(A.13)\quad R^{\sigma}_{(yz)} = \int_{-h/2}^{h/2} \sigma_{(yz)}(Df)\,dz = J_{44f}\gamma_y - \bar{J}^{e}_{24f}\phi_{,y}\,,$$

$$(A.14)\quad M^{\mu}_{[xy]} = \int_{-h/2}^{h/2} \mu_{xy}\,dz$$
$$= (-A^{b}_{33}/4)(w_{,xx}+w_{,yy}) + (E^{b}_{33f}/8)(\gamma_{x,x}+\gamma_{y,y})$$
$$- (\hat{F}^{a}_{33f}/2)\phi + A^{a}_{33}(V^0/h),$$

$$(A.15)\quad M^{\mu}_{[xz]} = \int_{-h/2}^{h/2} \mu_{xz}\,dz$$
$$= -(A^{b}_{22}/8)(u_{,xy}-v_{,xx}) - (A^{b}_{22f}/8)(\gamma_{x,xy}-\gamma_{y,xx})$$
$$+ (F^{b}_{22f}/8)\gamma_y + (\hat{E}^{a}_{22f}/2)\phi_{,y}\,,$$

$$(A.16)\quad M^{\mu}_{[yz]} = \int_{-h/2}^{h/2} \mu_{yz}\,dz$$
$$= -(A^{b}_{11}/8)(u_{,yy}-v_{,xy}) - (A^{b}_{11f}/8)(\gamma_{x,yy}-\gamma_{y,xy})$$
$$- (F^{b}_{11f}/8)\gamma_x - (\hat{E}^{a}_{11f}/2)\phi_{,x}\,,$$

$$(A.17)\quad R^{\mu}_{[xz]} = \int_{-h/2}^{h/2} \mu_{xz} f\,dz$$
$$= -(A^{b}_{22f}/8)(u_{,xy}-v_{,xx}) - (H^{b}_{22f}/8)(\gamma_{x,xy}-\gamma_{y,xx})$$
$$+ (L^{b}_{22f}/8)\gamma_y + (\hat{K}^{a}_{22f}/2)\phi_{,y}\,,$$

$$(A.18)\quad R^{\mu}_{[yz]} = \int_{-h/2}^{h/2} \mu_{yz} f\,dz$$
$$= -(A^{b}_{11f}/8)(u_{,yy}-v_{,xy}) - (H^{b}_{11f}/8)(\gamma_{x,yy}-\gamma_{y,xy})$$
$$- (L^{b}_{11f}/8)\gamma_x - (\hat{K}^{a}_{11f}/2)\phi_{,x}\,,$$

$$S^{\mu}_{[xy]} = \int_{-h/2}^{h/2} \mu_{xy}(Df)\,dz$$
$$= -(E^b_{33f}/4)(w_{,xx}+w_{,yy}) + (J^b_{33f}/8)(\gamma_{x,x}+\gamma_{y,y}) - (\bar{M}^a_{33f}/2)\phi + E^a_{33f}(V_0/h), \tag{A.19}$$

$$T^{\mu}_{[xz]} = \int_{-h/2}^{h/2} \mu_{xz}(D^2 f)\,dz$$
$$= -(F^b_{22f}/8)(u_{,xy}-v_{,xx}) - (L^b_{22f}/8)(\gamma_{x,xy}-\gamma_{y,xx}) + (N^b_{22f}/8)\gamma_y + (\hat{M}^a_{22f}/2)\phi_{,y}\,, \tag{A.20}$$

$$T^{\mu}_{[yz]} = \int_{-h/2}^{h/2} \mu_{yz}(D^2 f)\,dz$$
$$= -(F^b_{11f}/8)(u_{,yy}-v_{,xy}) - (L^b_{11f}/8)(\gamma_{x,yy}-\gamma_{y,xy}) - (N^b_{11f}/8)\gamma_x - (\hat{M}^a_{11f}/2)\phi_{,x}\,, \tag{A.21}$$

$$R^D_x = \int_{-h/2}^{h/2} (D_x)g\,dz$$
$$= -(\hat{E}^a_{11f}/4)(u_{,yy}-v_{,xy}) - (\hat{K}^a_{11f}/4)(\gamma_{x,yy}-\gamma_{y,xy}) - (\hat{M}^a_{11f}/4 - \bar{J}^e_{15f})\gamma_x + \hat{J}^{\eta}_{11f}\phi_{,x}\,, \tag{A.22}$$

$$R^D_y = \int_{-h/2}^{h/2} (D_y)g\,dz$$
$$= (\hat{E}^a_{22f}/4)(u_{,xy}-v_{,xx}) + (\hat{K}^a_{22f}/4)(\gamma_{x,xy}-\gamma_{y,xx}) - (\hat{M}^a_{22f}/4 - \bar{J}^e_{24f})\gamma_y + \hat{J}^{\eta}_{22f}\phi_{,y}\,, \tag{A.23}$$

$$T^D_z = \int_{-h/2}^{h/2} (D_z)(Dg)\,dz$$
$$= \hat{F}^e_{31f}u_{,x} + \hat{F}^e_{32f}v_{,y} - (\hat{P}^e_{31f} + \hat{F}^a_{33f}/2)w_{,xx} - (\hat{P}^e_{32f} + \hat{F}^a_{33f}/2)w_{,yy} + (\hat{L}^e_{31f} + \bar{M}^a_{33f}/4)\gamma_{x,x} + (\hat{L}^e_{32f} + \bar{M}^a_{33f}/4)\gamma_{y,y} + \hat{N}^{\eta}_{33f}\phi - \hat{F}^{\eta}_{33f}(2V_0/h), \tag{A.24}$$

where

$$(A.25)\qquad (A_{ij}\ B_{ij}\ D_{ij}\ A_{ijf}\ B_{ijf}\ D_{ijf}\ E_{ijf}\ F_{ijf}\ H_{ijf}\ J_{ijf}) = \int_{-h_m/2}^{h_m/2} \bar{c}_{ij}[1\ z\ z^2\ f\ zf\ z^2 f\ Df\ (D^2 f)\ f^2\ (Df)^2]\,dz,$$

in which the subscripts i and j are $i = j = 1,\ldots,6$ and $j = 1,\ldots,6$. $\bar{c}_{ij}$ are changed to c_{ij} when the pair of indices $(i,j) \neq (1,1),(1,2),(2,1)$ and $(2,2)$;

$$(A.26)\qquad \left(A^l_{kj}\ B^l_{kj}\ D^l_{kj}\ A^l_{kjf}\ B^l_{kjf}\ D^l_{kjf}\ E^l_{kjf}\ F^l_{kjf}\ H^l_{kjf}\ J^l_{kjf}\ K^l_{kjf}\ L^l_{kjf}\ M^l_{kjf}\ N^l_{kjf}\right) = \int_{-h/2}^{h/2} l_{kj}\Big[1\ z\ z^2\ f\ zf\ z^2 f\ Df\ (D^2 f)\ f^2\ (Df)^2\ f(Df)\ f(D^2 f)\ (Df)(D^2 f)\ (D^2 f)^2\Big]\,dz,$$

$$(A.27)\qquad \left(\hat{E}^l_{kjf}\ \hat{F}^l_{kjf}\ \hat{J}^l_{kjf}\ \bar{J}^l_{kjf}\ \hat{K}^l_{kjf}\ \hat{L}^l_{kjf}\ \hat{M}^l_{kjf}\ \bar{M}^l_{kjf}\ \hat{N}^l_{kjf}\ \hat{P}^l_{kjf}\right) = \int_{-h/2}^{h/2} l_{kj}\Big[g\ (Dg)\ g^2\ g(Df)\ gf\ (Dg)f\ g(D^2 f)\ (Dg)(Df)\ (Dg)(Dg)\ (Dg)z\Big]\,dz,$$

in which the subscript $k = 1,2,3$. The variables l_{kj} are changed to $\bar{l}_{kj}$ when $j = 3$. The variables l_{kj} are changed to a_{kk}, b_{kk}, and $c_{\alpha k}$ when $l = a$, b, and c, respectively. The variables l_{ij} are changed to e_{kj} when $l = e$, where $k = 1,2,3$, and $l = 1,\ldots,6$. $Dg = dg(z)/dz = -(\pi/h)\sin(\pi z/h)$.

References

1. H.F. TIERSTEN, *Linear Piezoelectric Plate Vibrations*, Plenum Press, New York, 1969.
2. S. KAPURIA, P. KUMARI, J.K. NATH, *Efficient modeling of smart piezoelectric composite laminates: a review*, Acta Mechanica, **214**, 31–48, 2010.
3. G.M. KULIKOV, S.V. PLOTNIKOVA, *Assessment of the sampling surfaces formulation for thermoelectroelastic analysis of layered and functionally graded piezoelectric shells*, Mechanics of Advanced Materials and Structures, **24**, 392–409, 2017.
4. D.A. SARAVANOS, P.R. HEYLIGER, *Mechanics and computational models for laminated piezoelectric beams, plates, and shells*, Applied Mechanics Reviews, **52**, 305–320, 1999.
5. J.I. WANG, J. YANG, *Higher-order theories of piezoelectric plates and applications*, Applied Mechanics Reviews, **53**, 87–99, 2000.
6. C.P. WU, Y.C. LIU, *A review of semi-analytical numerical methods for laminated composite and multilayered functionally graded elastic/piezoelectric plates and shells*, Composite Structures, **147**, 1–15, 2016.

7. C.P. Wu, K.H. Chiu, Y.M. Wang, *A review on the three-dimensional analytical approaches of multilayered and functionally graded piezoelectric plates and shells*, CMC-Computers, Materials & Continua, **18**, 93–132, 2008.

8. S.Q. Zhang, G.Z. Zhao, M.N. Rao, R. Schmidt, Y.J. Yu, *A review on modelling techniques of piezoelectric integrated plates and shells*, Journal of Intelligent Material Systems and Structures, **30**, 1133–1147, 2019.

9. G. Piazza, P.J. Stephanou, A.P. Pisano, *Piezoelectric, Aluminum Nitride vibrating contour-mode MEMs resonators*, Journal of Microelectromechanical System, **15**, 1406–1418, 2006.

10. G. Wingqvist, J. Bjurstrom, L. Liljeholm, V. Yantchev, I. Katardjiev, *Shear mode AIN thin film electro-acoustic resonant sensor operation in viscous media*, Sensors and Actuators B, **123**, 466–473, 2007.

11. T. Manzaneque, V. Ruiz-Diez, J. Hernando-Garcia, E. Wistrela, M. Kucera, U. Schmid, J.L. Sanchez-Rojas, *Piezoelectric MEMs resonator-based oscillator for density and viscosity sensing*, Sensors and Actuators A: Physical, **220**, 305–315, 2014.

12. R. Ardito, E. Bertarelli, A. Corigliano, G. Gafforelli, *On the application of piezolaminated composites to diaphragm micropumps*, Composite Structures, **99**, 231–240, 2013.

13. D.N.C. Nam, K.K. Ahn, *Design of an IPMC diaphragm for micropump application*, Sensors and Actuators A: Physical, **187**, 174–182, 2012.

14. O. Thoumine, A. Ott, O. Cardoso, J.J. Meister, *Microplates: a new tool for manipulation and mechanical perturbation of individual cells*, Journal of Biochemical and Biophysical Methods, **39**, 47–62, 1999.

15. J. Qiu, H. Ji, *The application of piezoelectric materials in smart structures in China*, International Journal of Aeronautical and Space Science, **11**, 266–284, 2010.

16. R.A. Toupin, *Elastic materials with couple-stresses*, Archive for Rational Mechanics and Analysis, **11**, 385–414, 1962.

17. R.D. Mindlin, H.F. Tiersten, *Effects of couple-stresses in linear elasticity*, Archive for Rational Mechanics and Analysis, **11**, 415–488, 1962.

18. W.T. Koiter, *Couple stresses in the theory of elasticity, I and II*, Philosophical Transactions of the Royal Society London B, **67**, 17–44, 1964.

19. A.C. Eringen, *Theory of Micropolar Elasticity*, in: H. Liebowitz [Ed.], Fracture, Academic Press, New York, 1968.

20. F. Yang, A.C.M. Chong, D.C.C. Lam, P. Tong, *Couple stress-based strain gradient theory for elasticity*, International Journal of Solids and Structures, **39**, 2731–2743, 2002.

21. B. Akgöz, Ö. Civalek, *Free vibration analysis for single-layered graphene sheets in an elastic matrix via modified couple stress theory*, Materials & Design, **42**, 164–171, 2012.

22. M. Mohammadi, M.F. Mahani, *An analytical solution for buckling analysis of size-dependent rectangular micro-plates according to the modified strain gradient and couple stress theories*, Acta Mechanica, **226**, 3477–3493, 2015.

23. H.T. Thai, D.H. Choi, *Size-dependent functionally graded Kirchhoff and Mindlin plate models based on a modified couple stress theory*, Composite Structures, **95**, 142–153, 2013.

24. G.C. TSIATAS, A.J. YIOTIS, *Size effect on the static, dynamic and buckling analysis of orthotropic Kirchhoff-type skew micro-plates based on a modified couple stress theory: comparison with the nonlocal elasticity theory*, Acta Mechanica, **226**, 1267–1281, 2015.

25. J. KIM, K.K. ZUR, J.N. REDDY, *Bending, free vibration, and buckling of modified couples stress-based functionally graded porous micro-plates*, Composite Structures, **209**, 879–888, 2019.

26. I. SHUFRIN, M. EISENBERGER, *Stability and vibration of shear deformable plates-first order and higher order analyses*, International Journal of Solids and Structures, **42**, 1225–1251, 2005.

27. H.T. THAI, S.E. KIM, *A size-dependent functionally graded Reddy plate model based on a modified couple stress theory*, Composites Part B, **45**, 1636–1645, 2013.

28. B. AKGÖZ, Ö. CIVALEK, *A microstructure-dependent sinusoidal plate model based on the strain gradient elasticity theory*, Acta Mechanica, **226**, 2277–2294, 2015.

29. Z.T. BENI, Y.T. BENI, *Dynamic stability analysis of size-dependent viscoelastic/piezoelectric nanobeams*, International Journal of Structural Stability and Dynamics, **22**, 2250050, 2022.

30. Y.T. BENI, *Size-dependent analysis of piezoelectric nanobeams including electro-mechanical coupling*, Mechanics Research Communications, **75**, 67–80, 2016.

31. M. JAFARI, E. JOMEHZADEH, M. REZAEIZADEH, *Length scale-dependent natural frequencies of piezoelectric microplates*, Journal of Vibration and Control, **24**, 2749–2759, 2018.

32. A. KAZEMI, R. VATANKHAH, M. FARID, *Vibration analysis of size-dependent functionally graded micro-plates subjected to electrostatic and piezoelectric excitations*, European Journal of Mechanics A/Solids, **76**, 46–56, 2019.

33. B. AKGÖZ, Ö. CIVALEK, *Modeling and analysis of micro-sized plates resting on elastic medium using the modified couple stress theory*, Meccanica, **48**, 863–873, 2013.

34. Q.H. PHAM, P.C. NGUYEN, *Dynamic stability analysis of porous functionally graded microplates using a refined isogeometric approach,* Composite Structures, **284**, 115086, 2022.

35. A. GHOBADI, Y.T. BENI, H. GOLESTANIAN, *Size-dependent thermo-electro-mechanical nonlinear bending analysis of flexoelectric nano-plate in the presence of magnetic field,* International Journal of Mechanical Sciences, **152**, 118–137, 2019.

36. A. GHOBADI, H. GOLESTANIAN, Y.T. BENI, *On the size-dependent nonlinear thermo-electro-mechanical free vibration analysis of functionally graded flexoelectric nanoplate*, Communications in Nonlinear Science and Numerical Simulation, **95**, 105585, 2021.

37. A.A. DEHKORDI, R.J. GOOJANI, Y.T. BENI, *Porous flexoelectric cylindrical nanoshell based on the non-classical continuum theory*, Applied Physics A, **128**, 478, 2022.

38. A. GHOBADI, Y.T. BENI, K.K. ZUR, *Porosity distribution effect on stress, electric field and nonlinear vibration of functionally graded nanostructures with direct and inverse flexoelectric phenomenon*, Composite Structures, **259**, 113220, 2021.

39. Q.H. PHAM, T.T. TRAN, V.K. TRAN, P.C. NGUYEN, T. NGUYEN-THOI, A.M. ZENKOUR, *Bending and hygro-thermo-mechanical vibration analysis of a functionally graded porous sandwich nanoshell resting on elastic foundation*, Mechanics of Advanced Materials and Structures, 2021, doi: 10.1080/15376494.2021.1968543.

40. Q.H. Pham, P.C. Nguyen, V.K. Tran, T. Nguyen-Thoi, *Finite element analysis for functionally graded porous nano-plates resting on elastic foundation,* Steel and Composite Structures, **41**, 149–166, 2021.

41. Q.H. Pham, T.T. Tran, V.K. Tran, P.C. Nguyen, T. Nguyen-Thoi, *Free vibration of functionally graded porous non-uniform thickness annular-nanoplates resting on elastic foundation using ES-MITC3 element*, Alexandria Engineering Journal, **61**, 1788–1802, 2022.

42. Q.H. Pham, P.C. Nguyen, T.T. Tran, *Dynamic response of porous functionally graded sandwich nanoplates using nonlocal higher-order isogeometric analysis*, Composite Structures, **290**, 115565, 2022.

43. J. Lou, L. He, J. Du, H. Wu, *Buckling and post-buckling analyses of piezoelectric hybrid microplates subjected to thermo-electro-mechanical loads based on the modified couple stress theory*, Composite Structures, **153**, 332–344, 2016.

44. M. Malikan, *Electro-mechanical shear buckling of piezoelectric nanoplate using modified couple stress theory based on simplified first order deformation theory*, Applied Mathematical Modelling, **48**, 196–207, 2017.

45. F. Abbaspour, H. Arvin, *Thermo-electro-mechanical buckling analysis of sandwich nanocomposite microplates reinforced with graphene platelets integrated with piezoelectric facesheets resting on elastic foundation*, Computers & Mathematics with Applications, **101**, 38–50, 2021.

46. H. Safarpour, Z.E. Hajilak, M. Habibi, *A size-dependent exact theory for thermal buckling, free and forced vibration analysis of temperature dependent FG multilayer GPLRC composite nanostructures resting on elastic foundation*, International Journal of Mechanics and Materials in Design, **15**, 569–583, 2019.

47. Y.S. Li, E. Pan, *Static bending and free vibration of a functionally graded piezoelectric microplate based on the modified couple-stress theory*, International Journal of Engineering Science, **97**, 40–59, 2015.

48. M.A. Abazid, M. Sobhy, *Thermo-electro-mechanical bending of FG piezoelectric microplates on Pasternak foundation based on a four-variable plate model and the modified couple stress theory*, Microsystem Technology, **24**, 1227–1245, 2018.

49. N.V. Nguyen, J. Lee, *On the static and dynamic responses of smart piezoelectric functionally graded graphene platelet-reinforced microplates*, International Journal of Mechanical Sciences, **197**, 106310, 2021.

50. I. Eshraghi, S. Dag, *Transient dynamic analysis of functionally graded micro-beams considering small-scale effects*, Archives of Mechanics, **73**, 303–337, 2021.

51. A. Razeghi-Harikandeei, B. Azizollah Ganji, R.A. Jafari-Talookolaei, A. Abdipour, *Static, free, and forced vibration analysis of a delaminated microbeam-based MEMS subjected to the electrostatic force*, Archives of Mechanics, **72**, 169–188, 2020.

52. I. Karimipour, Y.T. Beni, A.H. Akbarzadeh, *Modified couple stress theory for three-dimensional elasticity in curvilinear coordinate system: application to micro torus panels*, Meccanica, **55**, 2033–2073, 2020.

53. A.R. Hadjesfandiari, G.F. Dargush, *Couple stress theory for solids*, International Journal of Solids and Structures, **48**, 2496–2510, 2011.

54. A.R. HADJESFANDIARI, G.F. DARGUSH, *Fundamental solutions for isotropic size-dependent couple stress elasticity*, International Journal of Solids and Structures, **50**, 1253–1265, 2013.

55. A.R. HADJESFANDIARI, *Size-dependent piezoelectricity*, International Journal of Solids and Structures, **50**, 2781–2791, 2013.

56. F. ABBASPOUR, H. ARVIN, *Vibration and thermal buckling analyses of three-layered centrosymmetric piezoelectric microplates based on the modified consistent couple stress theory*, Journal of Vibration and Control, **26**, 1253–1265, 2020.

57. H. RAZAVI, A.F. BABADI, Y.T. BENI, *Free vibration analysis of functionally graded piezoelectric cylindrical nanoshell based on consistent couple stress theory*, Composite Structures, **160**, 1299–1309, 2017.

58. S. ZENG, B.L. WANG, K.F. WANG, *Static stability analysis of nanoscale piezoelectric shells with flexoelectric effect based on couple stress theory*, Microsystem Technology, **24**, 2957–2967, 2018.

59. C.P. WU, H.X. HU, *A unified size-dependent plate theory for static bending and free vibration analyses of micro- and nano-scale plates based on the consistent couple stress theory*, Mechanics of Materials, **162**, 104085, 2021.

60. Q. WANG, *On buckling of column structures with a pair of piezoelectric layers*, Engineering Structures, **24**, 199–205, 2002.

61. Q. WANG, S.T. QUEK, C.T. SUN, X. LIU, *Analysis of piezoelectric coupled circular plate*, Smart Materials and Structures, **10**, 229–239, 2001.

62. M.R. BARATI, H. SHAHVERDI, A.M. ZENKOUR, *Electro-mechanical vibration of smart piezoelectric FG plates with porosities according to a refined four-variable theory*, Mechanics of Advanced Materials and Structures, **24**, 987–998, 2017.

63. A. KARAMANLI, M. AYDOGDU, *Vibration of functionally graded shear and normal deformable porous microplates via finite element method*, Composite Structures, **237**, 111934, 2020.

64. N. SHAFIEI, S.S. MIRJAVADI, B.M. AFSHARI, S. RABBY, M. KAZEMI, *Vibration of two-dimensional impact functionally graded (2D-FG) porous nano-/micro-beams*, Computer Methods in Applied Mechanics and Engineering, **322**, 615–632, 2017.

Received September 18, 2022; revised version December 03, 2022.
Published online December 28, 2022.